

1 **Variations in Subsidence along the Gulf of Mexico passive margin from Airborne-**
2 **LiDAR data and Time Series InSAR in Louisiana**

3
4 **Carolina Hurtado-Pulido¹, Reda Amer², Cynthia Ebinger¹, Hayden Holcomb¹**

5 ¹Department of Earth and Environmental Sciences, Tulane University.

6 ²Lamar University, Beaumont, TX

7 Corresponding author: Carolina Hurtado-Pulido (dhurtadopulido@tulane.edu)

8 **Key Points:**

- 9 • Subsidence follows the spatial pattern of groundwater level changes from earlier studies,
10 uplift areas spatially relate to injection areas
11 • The Baton Rouge fault shows creep that likely accommodates changes in groundwater
12 level
13 • LiDAR differencing and SAR time series show similar vertical displacement trends. The
14 former is less precise but finds horizontal changes

15

16 **Abstract**

17 Coastal Louisiana is affected by sea level rates compounded by subsidence rates, leading to
18 flooding and land loss. Subsidence in the region is caused by natural and anthropogenic
19 processes that vary spatially and temporally across the Gulf of Mexico. Here, we quantify
20 modern vertical and horizontal displacement using InSAR time-series and LiDAR differencing
21 with data spanning between 1999-2020. Our study area is in Baton Rouge (BR), LA. It
22 encompasses two Quaternary faults that cut cemented Pleistocene sediments. We test the ability
23 of these methods to detect millimetric changes in an urban area with extraction and injection
24 wells. Both methods indicate that the footwall of the BR fault has larger subsidence values
25 (InSAR time series $\bar{x}=-0.552$ to -0.732 mm/y) than the hanging wall of the fault ($\bar{x}=1.94$ mm/y).
26 LiDAR differencing accurately detects displacement trends, although it can overestimate the
27 displacements. There are areas of uplift that spatially correlate to the locations of injection wells.
28 Our results indicate that subsidence follows the spatial pattern of groundwater level changes
29 proposed by previous studies, suggesting volumetric changes caused by fluid extraction and
30 injection. The correlation of the BR fault zone with the boundary between blocks subsiding at
31 different rates indicates that creep occurs along some sectors of the fault zone at rates of ~ 3
32 mm/y, similar to estimates from displaced structures. The creep may be accommodating changes
33 in groundwater level rather than gravity and salt dynamics. The fault zones may be more
34 permeable than surrounding areas, and more susceptible to hydrological and anthropogenic
35 processes.

36 **Plain Language Summary**

37 Coastal Louisiana is affected by sea level rise and surface sinking due to natural and human
38 activities. We used aerial and satellite data to measure the amount of ground sinking and uplift
39 between 1999 and 2020 in the metropolitan area of East Baton Rouge where sediments are stable
40 and two geological faults are crossing the region. We found that the whole area is experiencing
41 sinking, but the phenomenon is faster in the northern part than in the south of the study area
42 contracting expecting natural behavior. Our results relate uplift to the location and distribution of
43 wells injecting saline water and sinking relates to previous estimations of groundwater levels.
44 Our results should be considered for future urban planning and water management.

45 **1 Introduction**

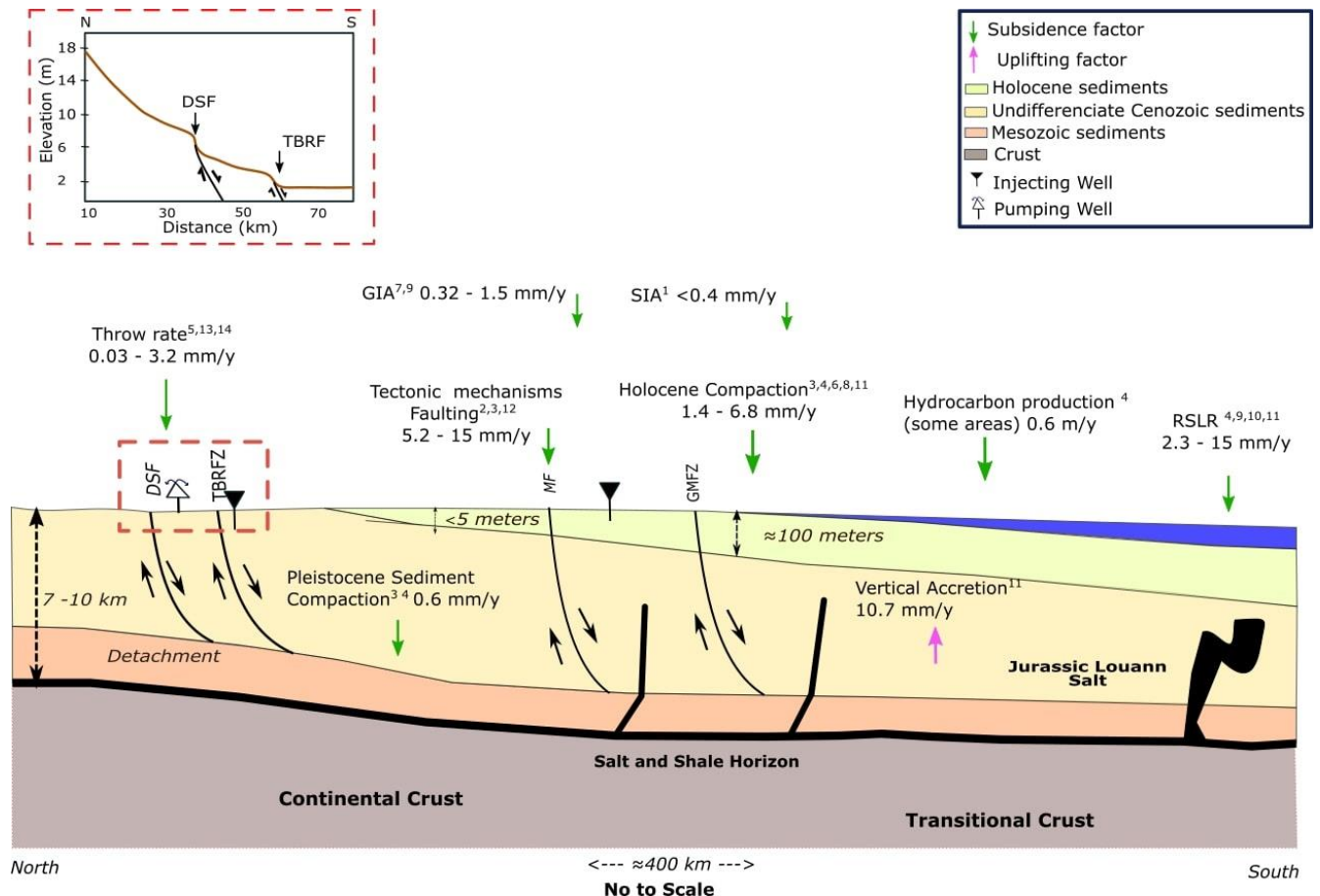
46 Climate change is modifying the natural systems of Earth. On a global scale, precipitation
47 patterns have changed, increasing evapotranspiration, as sea level rises mainly by thermal and
48 barystatic variations (Milliman and Haq, 1996; Frederikse et al., 2020). At local scales and
49 particularly in coastal areas, steric variations contribute greatly to sea-level changes (Frederikse
50 et al., 2020). At this scale, storm intensity and flooding increase as temperature rises (Milliman
51 and Haq, 1996; Church et al., 2013). During the 20th century, the global sea level increased
52 between 12-15 cm (Milliman and Haq, 1996), and it is expected to rise 65 ± 12 cm by 2100
53 (Hoffman et al., 1983; Church et al., 2013; Nerem et al., 2018). It will affect at least 190 million
54 people living mainly in coastal areas (Kulp and Strauss, 2019).

55 Relative sea-level (RSL), which includes sea-level rise and subsidence effects, has
56 increased along the Gulf of Mexico (GOM) coastline, causing great land loss. The mean RSL
57 rate along the coast of Louisiana is 10 - 12 mm/y, which is higher than global average estimates
58 of 1.2-3.3 mm/y (Penland and Ramsey, 1990; NASEM 2018a). Furthermore, the coast of
59 Louisiana is predicted to suffer more adverse consequences than other areas along the GOM due
60 to high rates of subsidence associated with the flood-controlled Mississippi delta (Pendleton et
61 al., 2010). Subsidence rates may surpass sea level rise rates in some regions (Nienhuis et al,
62 2017; Karegar et al, 2020).

63 Subsidence in southern Louisiana is caused by anthropogenic and natural processes such
64 as fluid extraction, compaction of recent sediments, isostatic adjustments, salt movement, and
65 faulting (NASEM, 2018b) (Fig. 1). The GOM is bordered by thick sedimentary basins
66 containing evaporites that overlie continental lithosphere stretched during Mesozoic time to form
67 the continental margin. Previous studies have quantified subsidence caused by compaction and
68 consolidation of compressible Holocene sediments of the Mississippi delta (e.g., Keogh and
69 Törnqvist, 2019; Karegar et. al., 2020). Fault slip and creep are difficult to quantify because they
70 can be episodic and slow, and the signal can be masked by faster processes such as
71 sedimentation (Gagliano et al., 2003b). Other researchers quantified local subsidence related to
72 the presence of fault traces and fluid extraction sites (e.g., Kuecher et al, 2001; Morton et al,
73 2002; Dokka, 2011). Mesozoic growth faults that detach in thick evaporite and shale horizons are
74 common in Louisiana, and several show evidence for Holocene slip. Yet, there are only three
75 instrumentally recorded earthquakes of M2.4-3.8 along the coastal fault systems (Stevenson and
76 Agnew, 1985; Walter et al., 2016), suggesting that slip occurs primarily by creep. Despite the
77 importance to infrastructure, there are just a few studies that have quantified fault slip rates and
78 their relationship with subsidence at different time scales in the area, with rates ranging between
79 0.03 – 16.9 mm/y (Gagliano et al., 2003a, 2003b; Dokka et al., 2006; Shen et al., 2016;
80 Culpepper et al., 2019a; Hopkins et al., 2021).

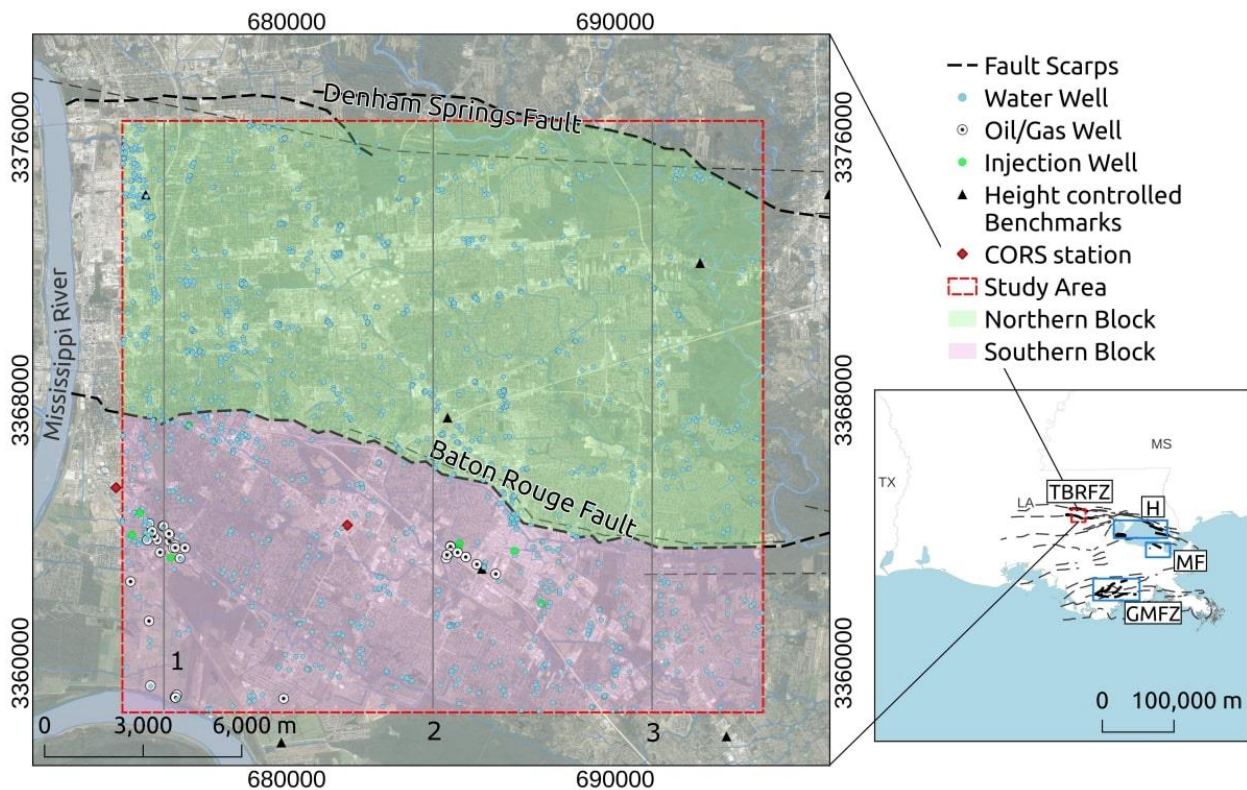
81 Differential movement along faults can be triggered in some areas by drivers such as
82 extraction or injection of fluids. Wells in Louisiana have multiple purposes like water, gas and
83 oil withdrawal, water injection and monitoring, with depths ranging between 4-6000 meters.
84 There are a large number of wells that may induce fault movement (Morton et al. 2002; Chan
85 and Zoback, 2007; Dokka, 2011; Jones et al., 2016). The change of pressure underground caused

86 by fluid extraction or injection changes the volume at depth, which could influence fault
 87 activation (Kuecher et al., 2001). Multiple studies have related extraction of fluids with
 88 subsidence at different locations (e.g., Jones et al., 2016, Puskas et al., 2017; Li et al., 2020;
 89 Guzy and Malinowska, 2020), and uplifting with injection of fluids (Shirzaei et al., 2016; Teatini
 90 et al., 2011). Interferometric Synthetic Aperture Radar (InSAR) technology has been used
 91 previously to detect local and regional variations in ground elevation in areas across the GOM
 92 (Jones et al., 2016; Fiaschi and Wdowinski, 2020) and has been recommended by the NASEM
 93 (2018a). Other studies have used Light Detection and Ranging (LiDAR) data of two different
 94 surveys to perform differential LiDAR to find ground changes using different techniques such as
 95 Iterative Closest Point (ICP) and DEM differences (Nissen et al., 2012; Scott et al., 2018;
 96 Wheaton et al., 2010; Neverman and Fuller, 2016).



97
 98 **Figure 1:** Schematic model of the extensional-contractional complex in southern Louisiana. After Shen et al. (2016)
 99 and Gasparini et al. (2015). Subsidence and uplifting references from: Kuchar et al. (2018)¹, Dokka et al. (2006)²,
 100 Dokka, (2006)³, Chan et al. (2007)⁴, Shen et al. (2016)⁵, Keogh and Törnqvist (2019)⁶, Love et al. (2016)⁷, Karegar
 101 et al. (2020)⁸, Karegar et al. (2017)⁹, Penland and Ramsey (1990)¹⁰, Jankowski et al. (2017)¹¹, Jones et al. (2016)¹²,
 102 Penland et al. (2001)¹³, Hopkins et al. (2021)¹⁴.

103 In this research we use LiDAR and SAR data spanning 1999-2020 to answer the
104 following questions: Assuming the 3 mm/y modern fault creep rate estimate by Hopkins et al.
105 (2020) for the faults across Lake Pontchartrain at ~50 km of the study area (Fig. 2), is it possible
106 to detect subsidence caused by fault slip with LiDAR and SAR? Are coastal growth faults
107 slipping and causing subsidence? Are areas of slip near fluid extraction and/or urban
108 development? We chose a test study area where two growth faults displace Pleistocene
109 sediments and the influence of Holocene sediment compaction and cementation is small to
110 isolate the signals of fault creep and anthropogenic change (e.g., Keogh and Törnqvist, 2019)
111 (Figs. 1, 2). Considering that LiDAR and InSAR time series have been successful in other
112 studies we decided to test LiDAR differencing in two faults in the Tepehate Baton Rouge fault
113 system, the Denham Springs and the Baton Rouge faults using airborne LiDAR data that spans
114 1999 to 2018 (Figs. 1, 2). We use two LiDAR surveys to apply differencing and SAR data from
115 Envisat and Sentinel-1 to apply Persistent Scatterer Interferometry (PSI). These techniques allow
116 one to determine continuous surfaces of elevation change, which enable us to detect subsidence
117 patterns in the study area. Comparing the results with well data, we can investigate where there is
118 fault slip, and whether there is a spatial correlation between fault slip and injection and extraction
119 wells over the last two decades. Answering these questions will let us verify or refute the
120 following hypotheses: 1) Differencing LiDAR surveys of different time periods can detect small
121 vertical motion signal with enough resolution of the two surveys, producing similar results to
122 InSAR, assuming there is vertical displacement close to 3 mm/y as suggested by Hopkins et al.
123 (2020) and 2) Tepehate Baton Rouge faults are slipping locally due to anthropogenic activities or
124 by natural causes, or a mix of both.



125
 126 **Figure 2:** Study area. Inset shows the location of the study area with respect to the Mississippi delta, surrounding
 127 states, and main fault systems in Louisiana. Michoud fault (MF), Golden Meadow fault zone (GMFZ) and the faults
 128 used by Hopkins et al. (2021) (H) are shown. Fault scarps from Culpepper et al. (2019b). Well data from the
 129 Louisiana Department of Natural Resources (SONRIS), (n.d.). Height controlled benchmarks and CORS stations
 130 from the National Geodetic Survey (n.d.). Gray lines and numbers are profiles for figure S3. Base map imagery from
 131 QuickMapServices - QGIS (Map data ©2015 Google).

132 1.1 Background

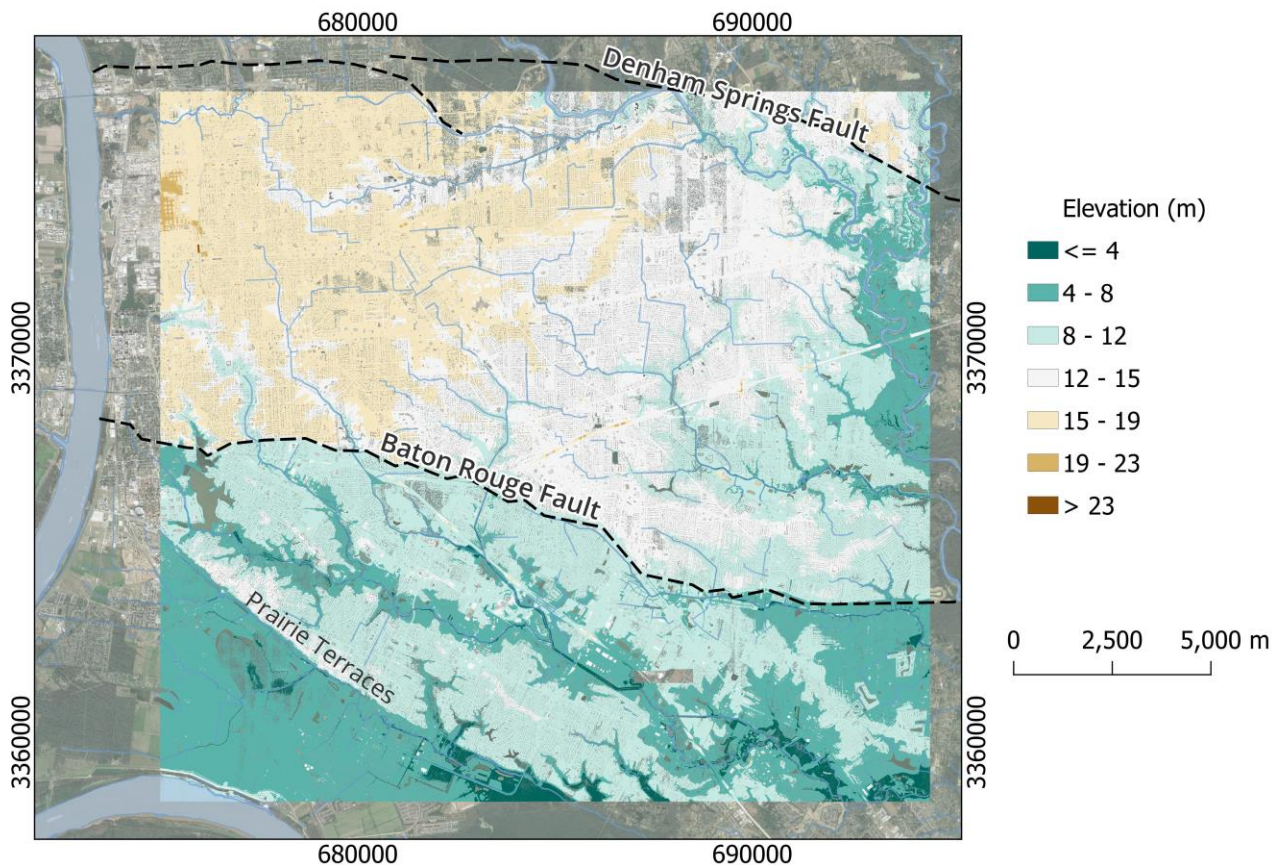
133 The GOM is a passive margin that formed between 200-158 Ma when the Pangea
 134 supercontinent tore apart due to extensional forces that created multiple normal faults (e.g.,
 135 Sawyer et al., 1991; Pindell and Kennan, 2009; Eddy et al., 2014). It is characterized by its bowl
 136 shape, low elevation coasts, broad continental shelf, followed by a steep continental slope, and a
 137 basin as deep as 4400 meters (e.g., Turner and Rabalais, 2019). The Mississippi River flows into
 138 the GOM, through the Mississippi delta (Figs. 1, 2). The delta began to develop at ~100 Ma with
 139 the formation of the Mississippi embayment, which concentrated sediment input to the gulf.
 140 During the last 7000 years, the delta depocenter relocated at least six times in response to climate
 141 and sea-level changes that occurred in the Holocene (Blum and Roberts, 2012). In the last 500
 142 years, the Mississippi delta has suffered drastic land loss. This could lead to a shift of the
 143 depocenter of the Mississippi delta caused by sea-level rise, climate change, anthropogenic

144 activities, and the lack of sediment delivery caused by artificial dams (e.g., Blum and Roberts,
145 2021).

146 Holocene sediment thickness increases from north to south and from west to east across
147 the coast of Louisiana and it reaches a thickness of 100 meters at the shoreline (Penland and
148 Ramsey, 1990). Processes such as compaction and compression of Holocene sediments are the
149 primary factors causing subsidence on the Mississippi delta, and in areas close to the shoreline
150 (Penland and Ramsey, 1990; Keogh and Törnqvist, 2019; Karegar et al., 2020). Keogh and
151 Törnqvist (2019) and Jankowski et al. (2017) found that shallow subsidence occurring in the
152 uppermost 5 meters in the Mississippi delta accounts for more than 60% of the total subsidence
153 in the coastal area with rates varying between 6.4 ± 5.4 and 6.8 ± 7.9 mm/y. Hence, we focus on
154 vertical crustal motions in areas north of the Holocene-Recent depocenter where compaction is
155 minor and where fault slip can be isolated. Faults in the Mississippi delta are listric faults that
156 commonly strike east-west (Dokka, 2011; Durham and Peeples, 1956; Culpepper et al., 2019).
157 Likely, these faults were active until 40 Ma, but their rate of slip decreased between 25 Ma until
158 the late Pleistocene (Shen et al., 2016). Our focus is the Tepeate-Baton Rouge fault system
159 (TBRFS), which has three faults each of which have several meters of topographic relief (Fig. 3)
160 (Denham Springs, Baton Rouge, and Scotlandville faults). These reactivated during the
161 Pleistocene due to rapid sedimentation rates (Shen et al., 2016; Culpepper et al., 2019). The relief
162 caused by Pleistocene-Recent slip along the TBRFS is clearly evident in DEMs produced from
163 LiDAR data (Fig. 3). Faults in this system merge at a depth of 6 kilometers into a detachment
164 that sits on an overpressured layer of salt and shale that dips with an angle between 45° to 65°
165 (Gagliano, 2003a; Shen et al., 2016) (e.g., Fig. 2). Movement at depth of salt deposits and
166 sediments can reactivate some fault segments (Gagliano et al., 2003a).

167 Studies differ in the importance of faulting as a factor causing subsidence in southern
168 Louisiana. Shen et al. (2016) calculated mean fault throw rates in the eastern portion of the
169 TBRFZ using optically stimulated luminescence dating to measure offset times and boundaries
170 of offset of fluvial/deltaic sediment facies. Their results indicate that faulting in the TBRFZ is
171 not a dominant process contributing to subsidence, given that the faults have an average slip
172 ranging between 0.02 -0.07 mm/y for areas lying on Pleistocene sites during the last 103 to 105
173 years. However, there is visual evidence of building and road displacements along the TBRFZ
174 and other coastal faults with measured rate estimates of ~ 3 mm/y (McCulloh, 2001; Hopkins et

175 al., 2021). Dokka et al. (2006a, 2006b) interpreted episodes of subsidence along the Michoud
 176 fault (MF) between 1955 to 2005 as evidence of episodic fault slip, although it could also be
 177 caused by groundwater extraction (Jones et al., 2016). Fault motion and subsidence near the
 178 Golden Meadow fault zone (GMFZ) have been related to hydrocarbon extraction in some studies
 179 (Morton et al., 2002; Chan and Zoback, 2007).



180
 181 **Figure 3:** Digital Elevation Model from the study area showing the topographic relief across the Denham Springs
 182 and East Baton Rouge faults (dashed lines). The geological contact labeled as the Prairie Terraces marks the edge of
 183 the natural levee in the area. Created using LiDAR point cloud from 2018. Base map imagery from
 184 QuickMapServices - QGIS (Map data ©2015 Google)

185 Glacial Isostatic Adjustment (GIA) and Sediment Isostatic Adjustment (SIA) may lead to
 186 long-term subsidence along the east coast of North America (Karegar et al., 2017). GIA was
 187 modeled using RSL data from tide gauges and vertical and horizontal velocities from GNSS
 188 from 2006-2015 along the East and Southeast coast of the United States by Love et al. (2016).
 189 During this century GIA in south-east Louisiana will contribute approximately 30 mm to RSL
 190 rise with a rate of 0.32 mm/y (Love et al., 2016). On the other hand, SIA registers a rate of less
 191 than 0.5 mm/y on areas with thicker Holocene sediments (Wolstencroft et al., 2014).

192 The aquifer system in Baton Rouge is part of the Southern Hills aquifer and the
193 Mississippi River Alluvial aquifer (Tomaszewski et al., 2002). The former is composed of
194 interbedded layers of compressed clay/silt and layers of porous sands. The sands south of the
195 Baton Rouge fault are more continuous than in the north area of the fault (Vahdat-Aboueshagh
196 and Tsai, 2021). These sands form ten independent aquifers named after their depth under the
197 Baton Rouge industrial district, with depths between 400-foot to 2700-foot (Tomaszewski et al.,
198 2002). Large volumes of groundwater removal have affected reservoirs in the Baton Rouge area
199 (White, 2017). Groundwater level has decreased forming cones of depression at local and
200 regional scales (White, 2017), and saline water from southern areas has intruded into some of
201 these sands (Nasreen, 2003; Elshall et al., 2013). Deep aquifers have larger withdrawal volumes,
202 and, therefore, have been more affected during the last decades (Tomaszewski et al., 2002;
203 Nasreen, 2003). The Mississippi River Alluvial aquifer has not had a significant groundwater
204 level decrease, and saline water has not infiltrated the eastern portion of the aquifer where the
205 study area is located (Tomaszewski et al., 2002; Nasreen, 2003). The Baton Rouge fault plays an
206 important role in the dynamics of the aquifers in Baton Rouge; it is a barrier for saline water
207 coming from the southern area, but it may serve as a conduit and can allow lateral intrusions due
208 to pumping of groundwater at the north of the fault (Nasreen, 2003; Elshall et al., 2013;
209 Anderson et al., 2013). The Denham Springs fault is permeable and allows freshwater to flow
210 down it to the south, where pressure gradients cause southward flow and aquifers in the area
211 between the two faults recharge (Elshall et al., 2013).

212 **2 Data**

213 Airborne LiDAR is a technique that uses laser light pulses directed towards Earth's
214 surface to measure the time of pulse return. This time is used to calculate the distance between
215 the sensor and the surface. Airborne LiDAR is used along with an airborne Global Navigation
216 Satellite System (GNSS) to know the location of the sensor while surveying and an Inertial
217 Measuring Unit (IMU) to know the angular orientation of the sensor relative to the ground
218 (Lillesand and Kiefer, 2000). SAR is a technique to capture data using microwave wavelengths.
219 The sensor on board the satellite or aircraft sends and receives signals that can penetrate haze,
220 clouds, snow, and smoke depending on the wavelength. SAR is particularly useful because it
221 simulates a longer antenna enabling the possibility of using long wavelengths and improving

222 spatial resolution (Lillesand and Kiefer, 2000; Chan and Koo, 2008). We utilize two data sets
223 spanning the longest time periods possible to detect vertical and horizontal land motion
224 associated with natural and anthropogenic processes in southern Louisiana.

225 **2.1 SAR data**

226 SAR datasets were captured by the EnviSAT and Sentinel-1 satellites. Both capture data
227 on the C-band (5.405 cm), produce Single-Look Complex images, we used vertical transmit and
228 receive polarization (VV). The EnviSAT dataset was collected between 2004 and 2010 and it is
229 composed of 23 scenes, this satellite has a mean incidence angle of 18, pixel dimensions of 5x25
230 m and has an altitude of 800 km (ESA, 2021a). The Sentinel-1 dataset was collected in
231 Interferometric Wide mode between 2017 and 2020 and consists of 33 scenes, Sentinel-1 has an
232 incidence angle between 37-39° and pixel dimensions of 14.1x2.3 m, and orbits at an altitude of
233 693 km (ESA, 2021b). Each of these datasets created a different time series that was analyzed
234 separately. For images list is on Table S1.

235 **2.2 LiDAR data**

236 LiDAR point clouds come from two surveys that cover the portion of the TBRZ fault
237 located in the East Baton Rouge parish in southern Louisiana. The first dataset was collected in
238 March of 1999, has a point space of 4 m, a pulse rate of 15 kHz and a vertical accuracy measured
239 as the Root Mean Square Error (RMSE) of 15 cm (USACE, 2001). The newest was collected
240 between March and April of 2018, has a point space of 0.33 m, a pulse rate of 450 kHz and a
241 vertical accuracy of RMSE=3.6 cm (USGS, 2019). For more details see Table S2.

242 **3 Methods**

243 **3.1 Persistent Scatter Interferometry - PSI (time series InSAR)**

244 PSI is a differential InSAR technique that allows one to use the phase information from
245 multiple SAR images captured at different times to estimate phase changes between several
246 interferograms. Phase change information is used to calculate the velocity of displacement and
247 the displacement time-series during the study period (Hooper et al., 2004; Crosetto et al., 2016).
248 PSI uses pixels with low phase noise, called Persistent Scatterers, across lengthy time intervals in
249 multi-temporal data (Ferretti et al. 2001; Crosetto et al., 2016). This technique is particularly

250 useful in urban areas that have a high density of persistent scatterers (e.g., Jones et al., 2016;
251 Fiaschi and Wdowinski, 2020). Displacement is calculated on the Line of Sight (LOS),
252 projecting 3D displacements into 1D displacements in the LOS direction (Crosetto et al., 2016).
253 One of the advantages of this technique is its ability to detect signals of ground displacements of
254 <10 mm/y (Lyons and Sandwell, 2003).

255 A brief description of this technique follows (L3Harris, 2014; 2021). One of the SAR images
256 from the stack is selected as a reference to co-register the other images and to create the time
257 series. Then, the interferometric process is implemented. This step includes co-registration and
258 interferogram generation between the reference image and the other images in the stack, as well
259 as interferometric flattening, where each interferogram is flattened. The topographic phase
260 component is prepared using a DEM to be subtracted from the total interferometric phase. Then,
261 reference points, which are persistent scatterers, are chosen using the Amplitude Dispersion
262 Index, defined as the temporal average amplitude of a pixel over temporal standard deviation of
263 the amplitude of a pixel.

264 After these preparation steps, the first inversion step is executed. This step calculates
265 displacement velocity and residual height using a linear model for each pixel in the area with
266 respect to the reference points selected above. The model estimates are removed from all the
267 interferograms to recalculate velocity and residual height. Next, the second inversion is applied.
268 At this step the atmospheric phase is estimated using a low and a high filter to remove spatial and
269 temporal variations caused by the troposphere from the interferometric phase. Next,
270 displacements are calculated from the clean interferometric phase for each interferogram. The
271 estimates for displacement and residual heights are recalculated and just pixels with coherence
272 larger than 0.66 (low phase noise) remain. The results are geocoded and exported to raster and
273 vector files.

274 We used SARscape software (version 5.6; 2021) to calculate vertical displacement velocity for
275 both datasets. The topographic phase was removed using the Shuttle Radar Topography Mission
276 (SRTM) DEM, which has a spatial resolution of 30 m. To reduce decorrelation noise and build
277 the spatial coherence map we ‘multilooked’, the data in azimuth and range directions as follows.
278 For the EnviSAT dataset we used four azimuth-looks and one range-look; for the Sentinel-1

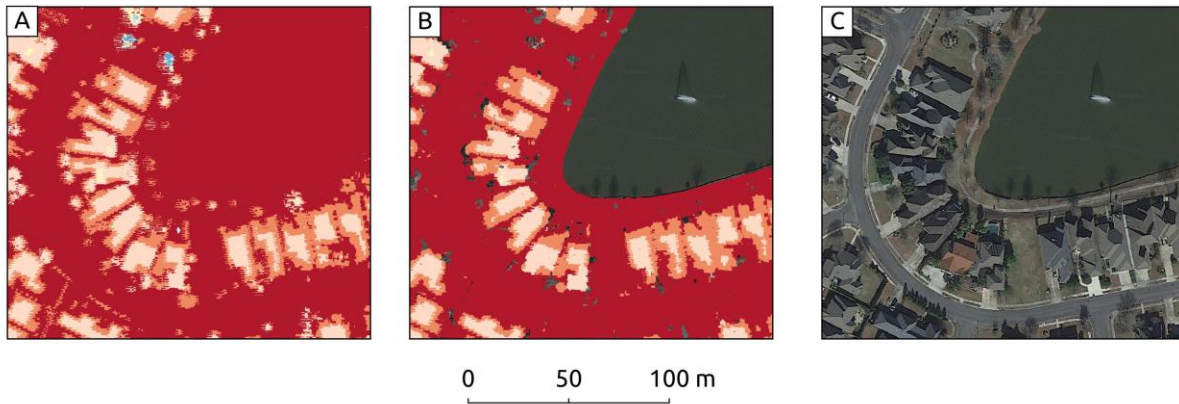
279 dataset we used five azimuth-looks and one range-look. This recombination reduces the quantity
280 of data to be processed but also decreases the spatial resolution (Goldstein et al., 1988). Only
281 pixels that fulfilled these threshold parameters were selected: 30% overlap for sub-areas, a single
282 reference point per 5 km², and coherence larger than 0.66. The PSI displacements are calculated
283 in the LOS direction. Then, we converted these to vertical displacements using the incidence
284 angle given as one of the results during the PSI process for each point. We assume that the
285 Earth's curvature does not affect the measurements.

286 **3.2 LiDAR co-registration**

287 Co-registration of the LiDAR point clouds is the process of aligning datasets acquired at
288 different times over the same area. Knowledge of the magnitude and the direction of the
289 misalignment enables us to detect horizontal displacements and correct the geographical location
290 of the point clouds to do vertical differencing between corresponding points. Misalignments
291 between the point clouds are caused by: 1) distortion of the point clouds from measurement error
292 related to flight discrepancies; 2) real changes in the landscape (subsidence, uplift, translation,
293 vegetation growth, mass movement); and 3) local topographic relief on flat surfaces where there
294 is less random LiDAR scattering (Scott et al., 2018).

295 Point cloud co-registration is done in two ways: using only LiDAR ground points and using
296 LiDAR points from structures that should be stable over time (e.g., flat roofs, parking lots, and
297 highways - Fig. 4). Ground points were taken using the original classification of both point
298 clouds done by the distributors. A feature-based technique allows us to take information from
299 structures that are expected to be stable and use them as control points (Brook and Ben-Dor,
300 2011). Using PDAL filters (Point Data Abstraction Library, 2018) we created a new point cloud
301 for each dataset whose points only belong to structures that satisfy specific criteria. First, the
302 point must be in a plane. To evaluate this criterion, we used the filter "estimatorank", which
303 categorizes each LiDAR point in a line, plane, or a 3D structure. The threshold value defines
304 whether a point is linearly independent or not. We used "estimatorank" with 14 neighbors and a
305 threshold value of 5 for the 1999 dataset and 1 for the 2018 dataset. Secondly, the points must be
306 in an elevation range assigned depending on if they are in the hanging wall or footwall of the
307 Baton Rouge Fault. The range for the hanging wall is 7 to 35 m and for the footwall is 12 to 35
308 m. These values were chosen from observation of the LiDAR data, using the maximum value

309 from tall buildings and the lowest from roads and parking lots. DEMs show that there are at least
 310 ~5 m of relief along the Baton Rouge fault (Fig. 3), therefore, features on the hanging wall are
 311 expected to be at a lower elevation.



312

313 **Figure 4:** Example of stable surfaces from 2018 LiDAR point cloud. (a) Original point cloud, (b) Chosen stable
 314 surfaces, (c) Reference image of the area. Base map imagery from QuickMapServices - QGIS (Map data ©2015
 315 Google)

316 **3.3 Iterative Closest point – ICP**

317 This algorithm allows one to perform 3D LiDAR differencing by calculating rotations and
 318 translations of the surface (Scott et al., 2018; Nissen et. al., 2012). The ICP algorithm aligns
 319 user-defined core points in the point clouds of two datasets. Each core point is defined by a grid
 320 of 50 m and centered in a square or window of 50x50 m in the 1999-point cloud and 51x51 m in
 321 the 2018-point cloud. We chose these values for computational optimization. The horizontal
 322 coordinates of each core are the central point in each window, and the elevation value is the
 323 average of all the points in the window. ICP assumes that each window behaves as a rigid body
 324 (Nissen et. al., 2012).

325 This algorithm iterates as follows: 1) Finds the closest core point in the old point cloud for each
 326 core point in the new point cloud, 2) Calculates translation and rotation of each core point in the
 327 old point cloud, 3) Iterates until a minimum distance is reached or until a certain number of
 328 iterations are completed (Scott et al., 2018; Nissen et. al., 2012). We iterated until the translation
 329 was less than 10⁻⁴ meters or when 10 iterations were completed. ICP applies a linear
 330 transformation to the old data to have the best alignment possible. It finds the rigid body
 331 transformation matrix, with α , β and γ representing the rotations on the x, y, and z axes, and

332 t_x, t_y, t_z representing the translations in the same three axes in equation 1 (Scott et al.,
333 2018).

$$334 \quad \mathbf{NewestPointCloud} \approx \mathbf{TransformedOldpointcloud} = \begin{pmatrix} 1 & -\gamma & \beta & t_x \\ \gamma & 1 & -\alpha & t_y \\ -\beta & \alpha & 1 & t_z \\ 0 & 0 & 0 & 1 \end{pmatrix} \mathbf{Oldpointcloud} \quad (\text{Eq. 1})$$

335 We run the ICP algorithm with LiDAR ground points and with LiDAR points from stable
336 surfaces chosen in the co-registration process. In both cases, approximately 122,400 core points
337 were created. The results of each core represent the displacement of a window. These results
338 were filtered to have only displacements between 0 to 1 m to eliminate outliers showing artifacts
339 (e.g., new constructions), and not natural displacements. Then, results were averaged to have a
340 representative point per 2.25 km². The error for this process is given initially by the Point-to-
341 Plane error metric (Scott et al., 2018; Nissen et. al., 2012), and the final averaged results were
342 evaluated using a margin of error metric of 95%. To perform differencing, we use the
343 3D_Differencing MATLAB code created by Scott et al., (2020) to apply ICP to topographic
344 data, and LIBICP (LIBRARY for Iterative Closest Point fitting) software created by Geiger et al.
345 (2011) to solve the rigid body transformation.

346 **3.4 Vertical DEM differencing**

347 To do vertical differencing we used Geomorphic Change Detection (GCD) software. It allows
348 one to detect topographic and volumetric changes using digital elevation models (DEM)
349 (Wheaton et al., 2010). With GCD we created a DEM of Differences (DoD) doing pixel by pixel
350 differentiation. The vertical accuracy of these is given by standard error propagation and depends
351 on the accuracy of the original point clouds (Wheaton, 2018). To implement GCD, the DEM
352 derived from the LiDAR point clouds is created using the PDAL filter “filters.range”, which
353 separates LiDAR points classified as ground from other levels, and then rasterizes this subset of
354 data using GDAL. We created the DEMs using the IDW (Inverse Distance Weighting)
355 interpolation technique, which is a linear combination of the samples, which weights them by
356 their distance to the point of interest. A radius can be used to choose only close points (Shepard,
357 1968; Polat et al., 2015). We used a pixel size of 5 m, and a radius of 5 m for the 1999-point
358 cloud and 3 m for the 2018-point cloud. The radius is different to ensure that the DEMs from
359 1999 have enough points to interpolate. We used a power parameter equal to 2 because it has

360 been shown to produce good empirical results and it is computationally efficient (Shepard,
361 1968). The error of each DEM with respect to the original LiDAR data was estimated using the
362 root mean square error metric.

363 **4 Results, or a descriptive heading about the results**

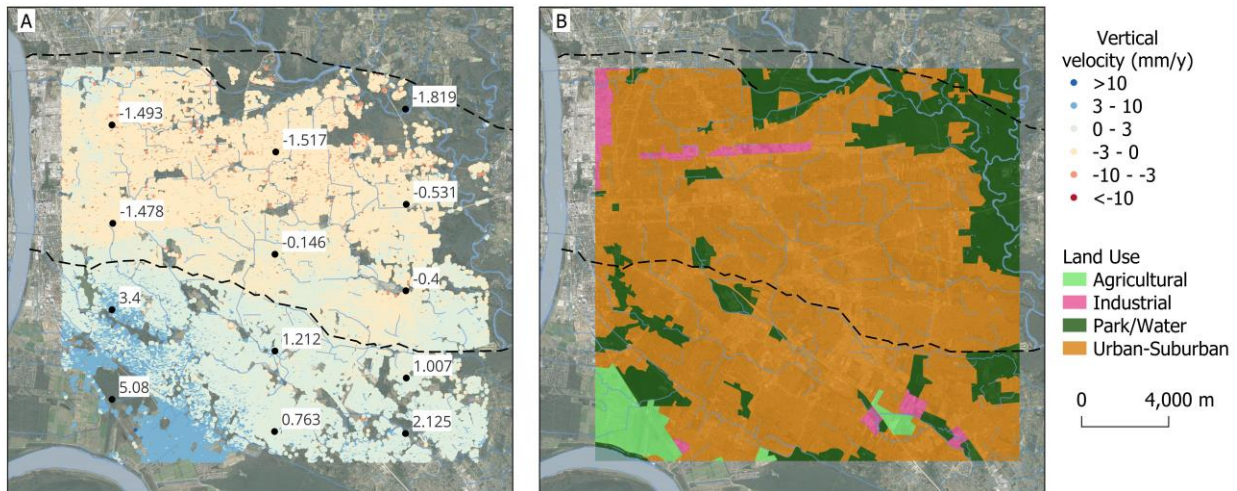
364 **4.1 Velocities from InSAR time series – Envisat and Sentinel-1**

365 The footwall of the Denham Springs fault does not show any results in the InSAR-time series
366 from Sentinel-1 (Fig. 5A), and the results from the EnviSAT are very noisy (Fig. 6). This area is
367 noisy in InSAR time series because most of the terrain is covered by vegetation and there are not
368 enough persistent scatterers (Fig. 5B).

369 For case of discussion, we will call the footwall block of the Baton Rouge fault northern block,
370 and the hanging wall of the Baton Rouge fault the southern block as indicated in Figure 1.

371 Results from InSAR time series using Sentinel-1 data captured between 2017 and 2020 indicate
372 that the northern block is moving in opposite sense to the long-term fault displacement, in other
373 words the subsidence rates in this block are larger than the ones found for the southern block
374 (Fig. 5A). Areas labeled as Agricultural, or Park/Water in Figure 5B do not have enough
375 persistent scatterers; therefore, we cannot produce results over these areas with this method. We
376 calculated a mean velocity value of -0.732 ± 0.004 mm/y for the northern block, which indicates
377 that subsidence dominates the block. The southern block has a mean velocity value of

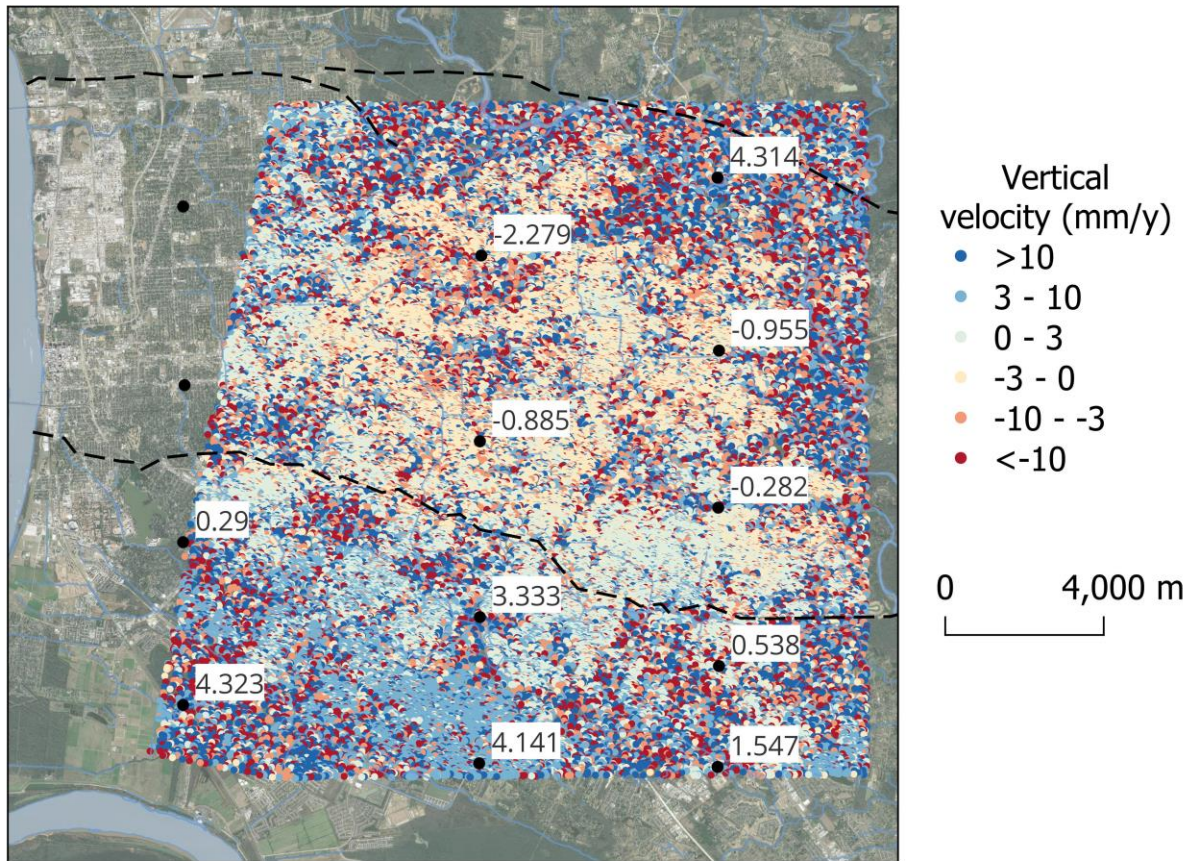
378 1.890±0.008 mm/y indicating that uplifting dominates the area. Errors in this section are
 379 presented as a margin of error within a confidence interval of 95%.



380
 381 **Figure 5:** Results from Sentinel-1 compared to Land use. **(a)** Vertical displacement rates calculated with PSI
 382 method. Labels on the image indicate mean vertical rates for the black dots. Negative velocities indicate subsidence
 383 while positive rate indicate uplifting. **(b)** Land uses. We mapped land uses using the basemap imagery from
 384 QuickMapServices - QGIS (Map data ©2015 Google.) at a scale of 1:10,000.

385 Figure 6 shows the spatial patterns of vertical displacement between 2004 and 2010 calculated
 386 with EnvisAT data. The results are noisy in many parts of the area, although we can see some
 387 patterns. The northern block has mean velocities of -0.552 ± 0.035 mm/y, indicating that most
 388 areas here are subsiding. On the other hand, the southern block has positive rates indicating
 389 uplift, with mean velocities of 2.007 ± 0.055 mm/y. The noise on the EnvisAT results may be
 390 caused by the resolution of the data and the lack of persistent scatterers in during the study

391 period. It also may be related to land-use changes during that period after Hurricane Katrina in
 392 2005. This will be further explained in the discussion section.



393
 394 **Figure 6:** Vertical displacement rates calculated with PSI method using Envisat data. Labels on the image indicate
 395 mean rates for the black dots to indicate how subsidence change over the area

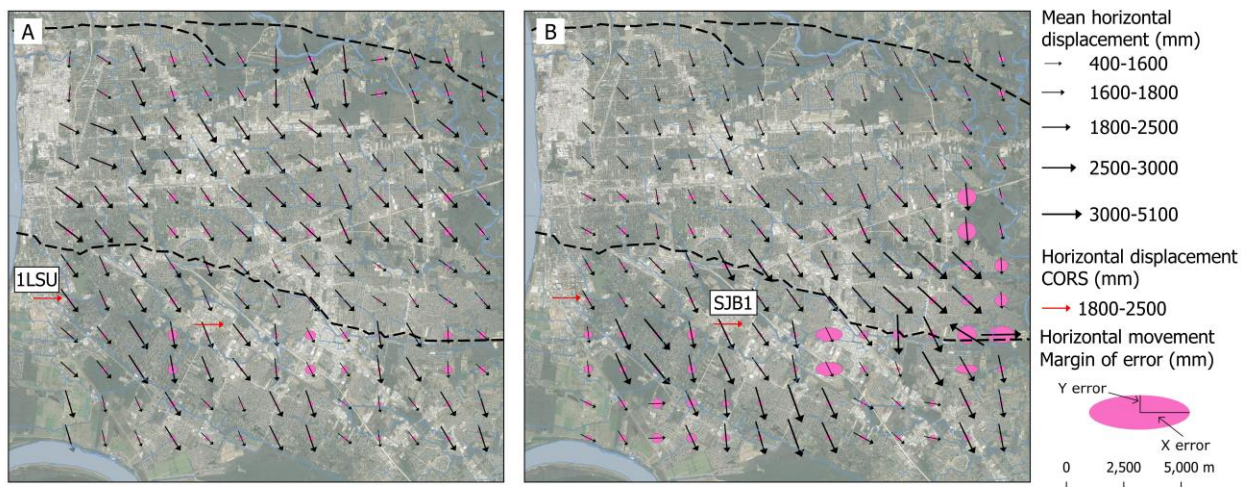
396 4.2 Horizontal displacement from ICP (Iterative Closest Point)

397 Overall, ICP indicates that between 1999-2018 the area is moved towards the southeast direction
 398 (Fig. 7). Results using the two different LiDAR classifications – ground and stable surface points
 399 – have different spatial behaviors. Horizontal displacement calculated with ground LiDAR points
 400 (Fig 7A) is spatially more homogenous in the whole area. Using ground points, we estimated that
 401 between 1999 and 2018, the mean displacement of the southern block was 148 ± 11 mm towards

402 the east and 85 ± 8 mm towards the south. The northern block has a mean displacement of
 403 145 ± 10 mm to the east and 110 ± 9 mm to the south.

404 The horizontal displacement calculated with stable LiDAR points shows different behaviors on
 405 each of the blocks (Fig. 7B); First, the southern block seems to be moving faster than the
 406 northern block with mean displacements of 178 ± 21 mm to the east and 91 ± 13 mm to the south,
 407 while the northern block had mean displacements of 121 ± 14 mm to the east and 81 ± 13 mm to
 408 the south. One particular feature of these results is that the areas closer to the eastern section of
 409 the Baton Rouge fault show large spatial variability and have larger errors. A caveat of using
 410 only stable surface points is that the number of these points is small, affecting mostly the oldest
 411 LiDAR survey.

412 Our results agree with the general estimated direction of displacement calculated with the two
 413 CORS stations in the study area (Fig. 7, Table 3). Between 1999 and 2018, the mean
 414 displacement with GNSS has a magnitude of approximately 239.21 mm to the east and 11.97
 415 mm towards the south. Our results also indicate large displacement towards the east (148-178
 416 mm), but displacements ~ 10 times larger towards the south (81-85 mm) for the study period.



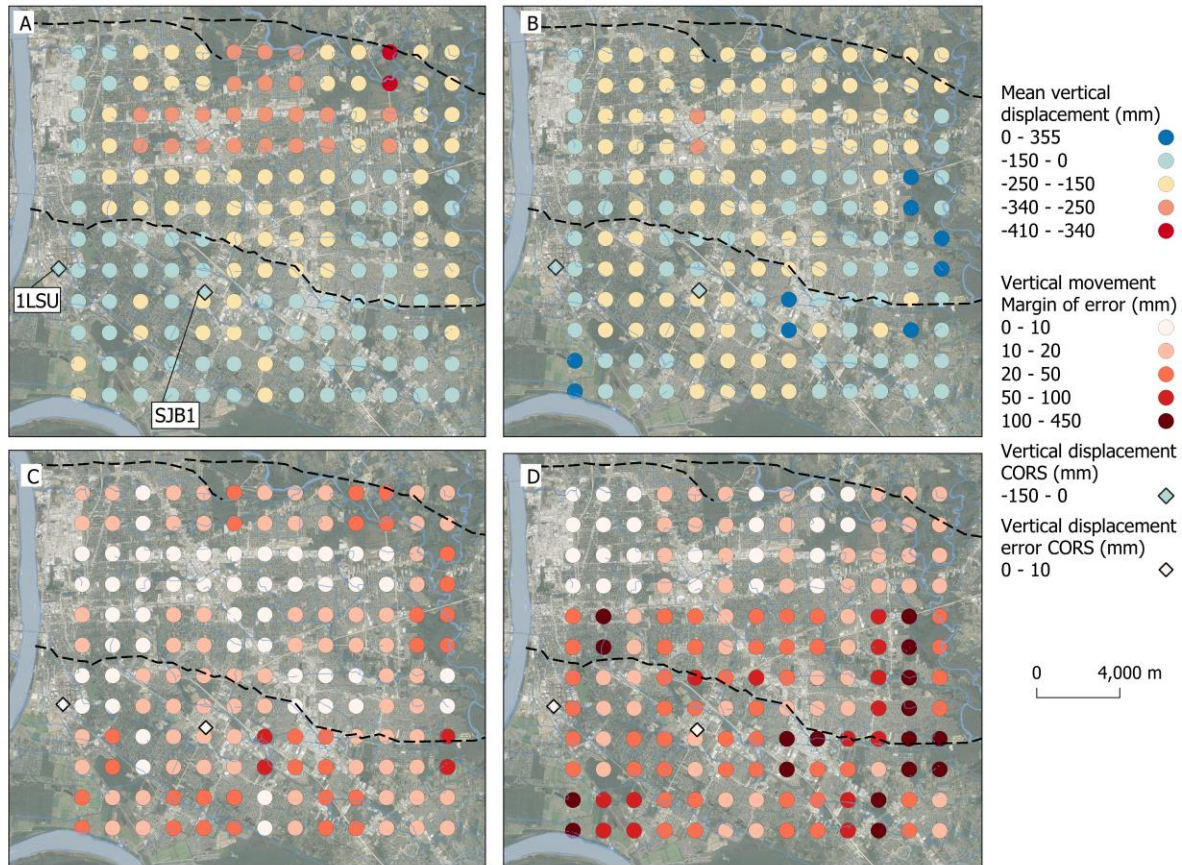
417
 418 **Figure 7:** Horizontal displacements calculated from ICP algorithm. (a) Horizontal displacements using ground
 419 LiDAR points. (b) Horizontal displacements using stable surface LiDAR points. Each black arrow represents the
 420 average displacement of an area of 2.25 km². Arrow directions represent the mean displacement direction, and the
 421 length of the arrow represents the mean displacement magnitude. Ellipses show the error multiplied by 30 for
 422 visualization, where X-error represents the error to the east and Y-error represents the error to the south. Errors are
 423 calculated as the margin of error with respect to the mean with a 95% of confidence limit. Red arrows are the
 424 horizontal displacement using the rates from the GNSS CORS stations for 19 years (1LSU, $V_x = -12.9 \pm 0.39$ mm/y,

425 $V_y = -0.54 \pm 0.3$ mm/y; SJB1, $V_x = -12.37 \pm 0.23$ mm/y, $V_y = -0.69 \pm 0.29$ mm/y). GNSS information from Nevada
426 Geodetic Laboratory GPS Network Map (Blewitt et al., 2018; UNAVCO, 2006), last access on December 6, 2021.

427 **4.3 Vertical displacement from LiDAR**

428 Both methodologies used to calculate vertical displacement with LiDAR data give us similar
429 results: subsidence is occurring across the study region, with larger subsidence in the northern
430 block. Uplifting regions are present in the southern block in the same areas that InSAR time
431 series shows them (Figs. 5, 6, 9, 10). Results from the ICP algorithm, where each point in Figure
432 8 represents the estimated displacement for an area of 2.25 km², shows that subsidence increases
433 from southwest to northeast. Using LiDAR ground points (Fig. 8A) there is no uplifting in large
434 regions as shown with PSI (Figs. 5, 6). The subsidence displacements in the southern block are
435 smaller in comparison to the displacements in the northern block. The mean vertical
436 displacement on the southern block is -131 ± 8 mm, and on the northern block is -193 ± 14 mm.
437 Now, using stable LiDAR points, we see some areas of uplift mostly on the southern block, and
438 again we estimate more subsidence in the northern block. The mean vertical displacement in the
439 southern block, in this case, is -103 ± 28 mm and on the northern block is -156 ± 20 mm. These
440 errors are margin of error within a confidence interval of 95%. ICP results are close to the
441 estimate displacement calculated with GNSS using the two stations in the southern block ($-$
442 44.365 mm using a vertical displacement mean rate of -2.355 mm/y, Fig. 8), assuming that the
443 vertical rate has been constant over time.

444

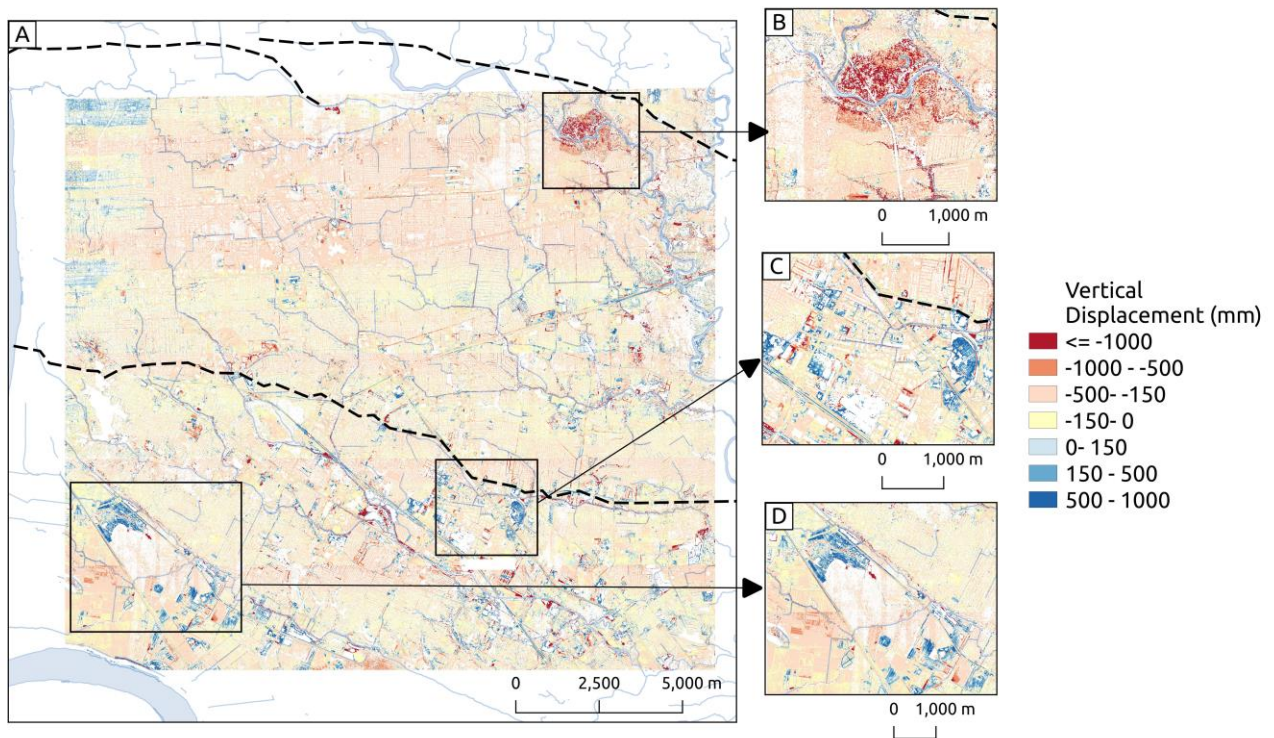


445

446 **Figure 8:** Vertical displacement calculated from ICP algorithm. (a) Vertical displacements using ground LiDAR
 447 points, (b) ICP displacements using stable surfaces LiDAR points, (c) Margin of error in the vertical direction for
 448 (a), (d) Margin of error in the vertical direction for (b). Each circle represents the average displacement of an area of
 449 2.25 km^2 . Errors are calculated as the margin of error with respect to the mean with a 95% of confidence. Rhombus
 450 are the vertical displacement calculated using rate from the GNSS CORS stations for 19 years (ILSU, $V_z = -$
 451 $3.86 \pm 0.84 \text{ mm/y}$; SJB1, $V_z = -0.85 \pm 0.79 \text{ mm/y}$). GNSS information from Nevada Geodetic Laboratory GPS
 452 Networks Map (Blewitt et al., 2018; UNAVCO, 2006), last access on December 6, 2021

453 We calculated LiDAR differencing with GCD without co-registration, with co-registration using
 454 ground points, and with co-registration using stable surface points. The mean estimates for
 455 vertical displacement without any co-registration for the 19 years were larger than 300 mm and
 456 we obtained more extreme values, which are not coherent with other estimates nor the features of
 457 the area. Therefore, we only keep the results from co-registered DEMs. We are presenting here
 458 just the results from LiDAR differencing co-registered with ground points (Fig. 9) because in
 459 these results are similar to the results from co-registration with stable points. In this case, we
 460 estimated a mean vertical displacement of $-118 \pm 0.00025 \text{ mm}$ on the southern block, and -
 461 $196 \pm 0.00015 \text{ mm}$ for the northern block. These errors are margin of error within a confidence
 462 interval of 95% and are small due to number of pixels in each block. Empty pixels on Figure 9

463 do not have results because there are water bodies, high vegetation density, or the values were
 464 below the propagated error calculated for each subarea of 2.25 km². Insets show areas of interest
 465 that will be discussed in the next section.



466
 467 **Figure 9:** Vertical displacements from LiDAR differencing using GCD. (a) Vertical displacement calculated using
 468 the DEM co-registered using the results from ground points co-registration for the complete study area. (b, c, d)
 469 Some areas of interest discussed in text.

470 All our estimations and main statistics are summarized in Table 1 below.

471 Table 1: Main statistics for PSI rates, LiDAR differencing from ICP and GCD and GNSS. MOE stands for Margin
 472 of Error.

PSI – Estimate vertical displacement rates						
Dataset	Time span	Block	Mean (mm/y)	Median (mm/y)	MOE (mm/y)	Mean displacement (mm)
EnviSAT	2004-2010	Northern	-0.552	-0.872	0.035	-3.864
		Southern	2.007	2.179	0.055	14.049
Sentinel-1	2017-2020	Northern	-0.732	-0.726	0.004	-2.928
		Southern	1.890	1.667	0.008	7.56

ICP – Estimate displacement (1999 -2018)						
Point cloud	Variable	Block	Mean (mm)	Median (mm)	MOE (mm)	Mean rate (mm/y)
Ground	Vertical	Northern	-193	-175	14	-10.178
	X (east)		145	141	10	7.642
	Y (south)		-110	-112	9	-5.782
	Vertical	Southern	-131	-138	8	-6.879
	East		148	151	11	7.789
	South		-85	-90	8	-4.471
Stable	Vertical	Northern	-156	-177	20	-8.213
	X (east)		121	102	14	6.389
	Y (south)		-81	-59	13	-4.252
	Vertical	Southern	-103	-143	28	-5.429
	X (east)		178	177	21	9.366
	Y (south)		-91	-95	13	-4.770
GCD – Estimated vertical displacement (1999 -2018)						
Block	Mean (mm)	Median (mm)	MOE (mm)	Mean rate (mm/y)		
Northern	-196	-192	0.00015	-10.339		
Southern	-118	-153	0.00025	-6.194		
GPS –Rates and displacements (1999-2018)						
Mean rate - vertical (mm/y)	-2.335	Mean displacement vertical (mm)	-44.365			
Mean rate - X (mm/y)	12.59	Mean displacement X (mm)	239.21			
Mean rate - Y (mm/y)	-0.63	Mean displacement Y (mm)	-11.97			

473 **5 Discussion**474 **5.1 InSAR time series and LiDAR differencing measurements**

475 InSAR time series created with the PSI method calculated rates of displacement in the LOS
476 direction. We translated LOS displacement to vertical displacement using the incidence mean

477 angle for each point in the results. This technique uses persistent scatterers on the surface,
478 making this methodology appropriate for urban environments with a high density of scatterers,
479 such as Baton Rouge. One must be cautious, however, with the interpretation of these results
480 because they incorporate the signal of all processes affecting the persistent scatterers (Jones et
481 al., 2016). Each time-series was calculated using images from different dates; therefore, vertical
482 displacement rates may be affected by seasonal variations from the hydrological cycle (e.g., Li et
483 al., 2020). Most of the images that we used from EnvisAT and Sentinel-1 were captured during
484 dry periods in Baton Rouge (September to May) and some from wetter periods. If there is any
485 elastic deformation caused by seasonal changes in water mass, it would be more positive than
486 negative due to the time distribution of the images. Seasonal loading, therefore, may contribute
487 to the observed uplift in the southern block for both time series (Fig. 5 and 6). If the observed
488 uplift of our results is caused by seasonal rebound, then subsidence rates may be larger than the
489 ones reported with InSAR time series, this based in comparison to hydrological models (e.g.,
490 Puskas et al., 2017).

491 We also used two LiDAR surveys captured over similar seasonal conditions to perform LiDAR
492 differencing (Table 2). Therefore, this method probably measured net changes between both
493 surveys, although uncertainties in each survey must be considered. In this case, the survey taken
494 in 1999 affects the displacement estimates more than the survey from 2018 due to the sparsity of
495 the point cloud. LiDAR allows one to use data from surfaces of interest such as ground and
496 stable surfaces points separately. The advantage of using different LiDAR points is shown in
497 Figures 7 and 8, where surfaces that are at different elevations or anchored in the subsurface
498 report distinct behavior of displacement in some zones of the study area. The estimated
499 horizontal displacement indicates that the study area moves towards the southeast in both blocks
500 (Fig. 7) agreeing with the geological characteristics of listric faults across the gulf (Culpepper et
501 al., 2019). Nevertheless, horizontal displacements estimated with stable LiDAR points (Fig. 7B)
502 have smaller displacements in the northern block than in the southern block. These
503 displacements have more variations than those calculated with ground points, particularly near
504 the eastern segment of the Baton Rouge fault (Fig. 7A). These differences between results from
505 ground and stable LiDAR points may indicate anomalies close to the fault, but also may be

506 caused by the lack of stable surfaces in some areas in 1999 before rapid urban growth between
507 2005-2010.

508 **5.2 Comparison LiDAR differencing, time series InSAR and GPS records**

509 InSAR time series and LiDAR differencing indicate that the northern block is subsiding faster
510 than the southern block, with the fault serving as a clear boundary between the uplifting and
511 subsiding zones. The uplift, however, contradicts the long-term displacement of the down-to-
512 south normal fault. Mean subsidence rates from LiDAR differencing (-8.213 - -10.339 mm/y) are
513 one to two orders of magnitude larger than the rates calculated with InSAR time series (-0.552 - -
514 0.732 mm/y) for the northern block (Table 3) clearly indicating the lower accuracy of the LiDAR
515 data. Yet, regional patterns are similar: the northern block is subsiding. Now, our results for the
516 southern block differ between methods. Mean rates from InSAR time series show that this block
517 is mostly uplifting, while LiDAR differencing mean rates indicates that the southern block is
518 subsiding but at a slower rate than the northern block, with some spatial patches of uplift (Table
519 3, Fig. S1). As explained above, InSAR time series may be affected by seasonal changes, which
520 would bias results to uplift. In the southern block, there are two GNSS stations, 1LSU and SJB1,
521 continuously working since 2004 and 2010, respectively (Fig. 8), but they were mounted on
522 buildings with unknown foundations. GNSS data indicate that this block is experiencing
523 subsidence as indicated by LiDAR differencing, although the rates from GNSS are ~2.5x smaller
524 than the rates from LiDAR, but slightly larger than those from InSAR time series. GNSS
525 indicates that horizontal displacement of the area is to the south-east direction similar to LiDAR
526 differencing. Although the magnitude to the south direction is larger with LiDAR differencing,
527 and smaller to the east direction (-4.471 mm/y to the south and 7.789 mm/y to the east with
528 LiDAR differencing with ground points and -0.63 mm/y to the south and 12.59 mm/y to the east
529 with GNSS data – Table 3).

530 InSAR time series and LiDAR differencing showed similar results in trends and are comparable
531 to GNSS estimations, which corroborates their usefulness to estimate slow deformation for
532 future studies (Fig. 5-9). LiDAR differencing results have a larger magnitude but have a better
533 spatial resolution, while InSAR time series has better temporal resolution with good spatial
534 resolution compared to point methods such as GNSS. InSAR time series has the advantage of

535 openly available data from different satellites that cover the globe almost completely and there
536 are multiple software options to process the data (e.g., SARscape, ISCE, GMTSAR).

537 **5.3 Relation with anthropogenic activities**

538 Results from LiDAR differencing are estimators for trend motions with good spatial resolution to
539 detect changes in small areas. For instance, construction of the FedEx facility (2014), the
540 Ochsner Medical Complex (2017), the Woman's Hospital (2010), and some new home
541 complexes (2006-2017) are seen in Figures 9C and 9D. We consider that urban growth and new
542 constructions cannot cause this wide and large uplift signal because urban growth has occurred
543 across Baton Rouge including the northern block, where we found multiple examples of new
544 constructions with similar characteristics that do not show this type of uplifting (Fig. S2). The
545 2000, 2010, and 2020 censuses indicate that the city's population has increased by almost 10%
546 (close to 40,000 new habitants) with most of this increase occurring during the first decade and
547 soon after Katrina when many were displaced (U.S. Census Bureau, 2003; U.S. Census Bureau,
548 2012; U.S. Census Bureau, 2021). Uplift recorded in LiDAR-differencing is also shown in both
549 InSAR time series, though the last one shows wider uplifting areas.

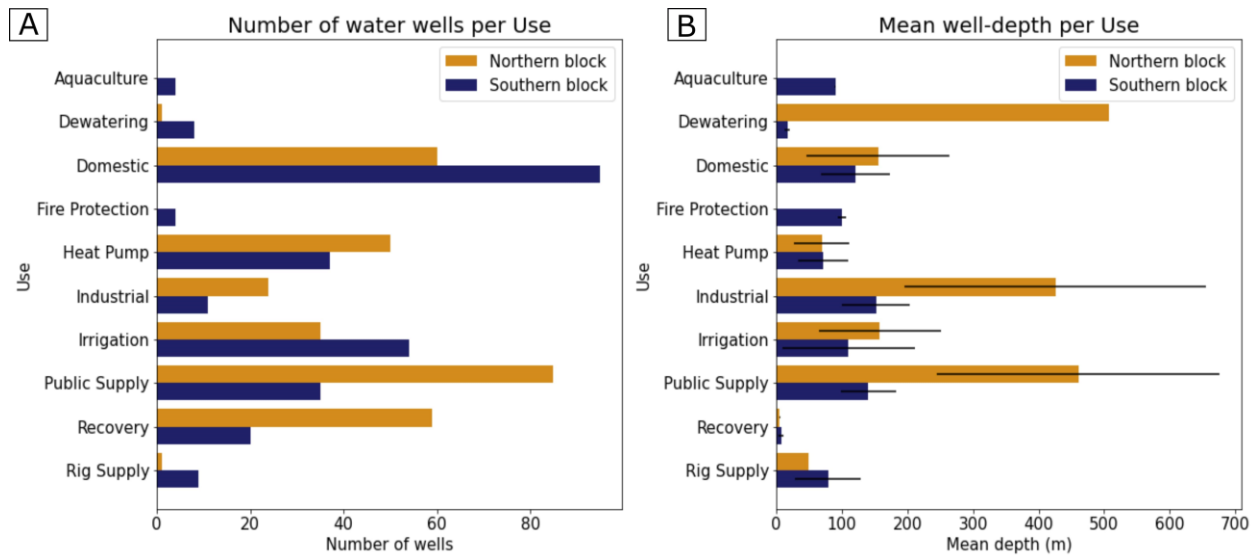
550 Using the SONRIS database (n.d.), we counted and categorized wells to know if there is a spatial
551 relationship between wells' locations, construction, and our results. For this analysis, we used
552 wells that were active in any period between 1999 and 2021. Wells that did not have information
553 about starting or ending operation dates were not used. We did not analyze injection pressure or
554 rate of injection or extraction because most of the wells have incomplete information about these
555 data. However, wells that were operating before in the study area can, in some cases, cause
556 delayed pore pressure changes and deform the surface (Shirzaei et al., 2016).

557 During the study period 2034 water wells were active: 1359 of the wells were in the northern
558 block, and 675 were in the southern block. In total 616 wells extract groundwater for different
559 purposes (Fig. 10), and the remaining 1418 wells monitor groundwater quality mostly near
560 industrial wells, close to areas of injection or oil extraction, and near the western section of the
561 Baton Rouge fault. Most of the groundwater in East Baton Rouge is used for industrial and
562 public supply. These uses are recognized to cause most of the decline of the groundwater levels
563 in the parish (Tomaszewski et al., 2002). Groundwater studies indicate that aquifers in the

564 northern block recharge from water infiltration in areas north of the Denham Springs fault (e.g.,
565 Tomaszewski et al., 2002; Vahdat-Aboueshagh and Tsai, 2021). It is known that the withdrawal
566 of groundwater in the Baton Rouge district surpasses the recharge of the aquifers, causing a
567 decline in groundwater levels (White, 2017). The amount of water wells in the northern block is
568 larger for almost all uses than in the southern block (Fig. 10A). Also, most wells are at deeper
569 depths in the northern block (Fig. 10B). Water well data shows that the mean depth of industry
570 and public supply wells is between 400-500 m (1312.34-1640.42 ft), probably reaching the 1500-
571 to 2000-ft sands. These aquifers have been greatly affected by pumping water (Tomaszewski et
572 al., 2002; Nasreen, 2003; Elshall et al., 2013). On the other hand, the southern block has fewer
573 water wells extracting water, but it has injection wells that may cause some uplift by increasing
574 the pore pressure at depth, and the aquifers here receive saline water from the south (Anderson et
575 al., 2013).

576 Jones et al. (2016) concluded that groundwater withdrawal caused subsidence in the Michoud
577 area in New Orleans, and other studies support this relationship in other areas (eg., Guzy and
578 Malinowska, 2020; Fiaschi and Wdowinski, 2020). They found that areas around chemical plants
579 or refinery facilities with water wells have large subsidence rates. Figure 9B shows the area with
580 the largest subsidence in the study area. This subsidence zone is detected by LiDAR
581 differencing, whereas in InSAR time series it is masked by dense vegetation during the analyzed
582 period. This area does not have water wells, but 12 water wells were active during the study
583 period within a radius of 2 km, eight of which are of domestic use located at the north and east,
584 three for public supply to the west, and one for irrigation also to the west (Fig. S2). Besides this
585 area, we did not find specific water wells linked to anomalous subsidence. Due to the large
586 amount and depth at which the water wells bottom in the northern block in comparison to the
587 water wells in the southern block and considering previous analyses of groundwater withdrawal
588 in the area, our study suggests that the northern block is part of a regional depression cone
589 caused by water extraction. To corroborate this, it is necessary to expand the study area, which is

590 possible to do using SAR data, but the available LiDAR data does not cover the eastern and
 591 western portions.



592
 593 **Figure 10:** Water wells statistics per block in the study area. (a) Number of water wells per use. (b) Mean depth of
 594 water wells per use, black lines are error bars of one standard deviation. Well data from the Louisiana Department of
 595 Natural Resources (SONRIS), (n.d.).

596 The areas of new construction in Figure 9C and 9D were selected not only because they have the
 597 largest uplift signal in the study area but also because most injection wells and oil/gas extraction
 598 wells considered for this study are close to or inside these zones (Fig. 1). There are 12 injection
 599 wells in the study area, and all are located in the southern block. Nine of these injected salt water
 600 at depths between 1470-1975 meters and are in the areas shown in Figures 9C and 9D. The other
 601 three inject ozone at shallow depths (~15 m) and are not in any of these areas. Multiple studies
 602 have shown that injection can increase pore pressure at depth which can diffuse and cause
 603 uplifting (e.g., Shirzaei et al., 2016; Teatini et al., 2011). This increase of pressure can be an
 604 explanation for the observed uplift in the southern block.

605 **5.4 Geological factors**

606 The study area has multiple factors that may contribute to vertical crustal movement and are
 607 difficult to detangle, but sediment compaction is minimal. Our LiDAR and InSAR results show
 608 that the Baton Rouge fault marks the boundary between faster and slower subsiding areas, but we
 609 cannot determine whether parts or all of the fault zone slipped episodically or continuously
 610 between 1999 and 2020. The rates of differential motion (~3 mm/y) we determine are two orders

611 of magnitude larger than the time-averaged fault slip rate of Shen et al. (2016), These results
612 are comparable to the ~ 3 mm/y rates along some segments of the Baton Rouge fault reported by
613 Hopkins et al. (2020), suggesting that anthropogenic activities have increased slip rates.

614 The ICP results from the eastern portion of the Baton Rouge fault shows an apparent change in
615 horizontal displacement direction, but uncertainties are also large. This can be an area for future
616 research because it is also close to two oil fields in the south, these have four injection wells and
617 11 oil/gas extraction wells that extract from the Siegen field (SONRIS, n.d.). Also, this fault
618 segment is the closest to the study area of Hopkins et al., (2020) (Fig. 2). We cannot conclude
619 much about how the Denham Springs fault is causing subsidence due to the lack of information
620 in the area.

621 Due to large volumes of groundwater withdrawal in the northern block there is the possibility
622 that some of this saline water is crossing the fault (Nasreen, 2003; Elshall et al., 2013; Anderson
623 et al., 2013) infiltrating some aquifers near the Baton Rouge fault in the northern block. This
624 may explain our general pattern of vertical displacements where subsidence increases from south
625 to north with InSAR time series and LiDAR differencing.

626 **5.5 Future Implications**

627 The vertical crustal motion that occurred during the last two decades detected with InSAR time-
628 series and LiDAR differencing and corroborated by sparse GNSS data can be an indicator of
629 groundwater level and recharge characteristics for the aquifers under the study areas. The
630 aquifers in the northern block are more affected by groundwater extraction. This block has
631 subsidence rates that decrease towards the Baton Rouge fault where saline water infiltrates
632 (Nasreen, 2003; Elshall et al., 2013). The southern block is also undergoing subsidence, but
633 injection causes uplift, and recharge of the aquifers in this block is faster due to saline water flow
634 from southern areas (Fig. 5, 6, 8, 10). Therefore, it is important to perform continuous
635 monitoring at local and regional scales to know how the area is affected by fluid extraction and
636 injection. There are many wells whose purpose is to monitor locally groundwater health, and
637 there are just a few GNSS stations to examine surface changes. This study presents a detailed

638 regional panorama of the relationship between injection and extraction of fluids and vertical
639 surface motion.

640 East Baton Rouge is one of the most populated parishes in Louisiana and likely its population
641 will grow as has done it for the last 20 years according to the censuses since 2000 (U.S. Census
642 Bureau, 2003; U.S. Census Bureau, 2012; U.S. Census Bureau, 2021). Besides, due to climate
643 changes expected for the ongoing century in the GOM (Pendleton et al., 2010; Frederikse et al.,
644 2020) some population from the Louisiana coastal area probably will migrate to this parish to
645 avoid areas that are at lower elevation and are more vulnerable to flooding (Qiang and Lam,
646 2016) or after hurricanes, as has happened before (Sastry, 2009). Thus, water consumption
647 probably will increase as the population increases. Considering subsidence as a proxy for
648 groundwater levels, it is important to protect the aquifers underlying the area from saline
649 intrusion and groundwater level decline. These actions will also protect the surface from non-
650 natural vertical changes.

651 **6 Conclusions**

652 We used InSAR time series and LiDAR differencing to evaluate vertical and horizontal crustal
653 movements along the Gulf of Mexico passive margin, including an area of ongoing movement
654 along growth faults between 1999 and 2020. The comparison of methods offers insights into the
655 reliability of differential LiDAR in coastal subsidence. The study area has two listric faults that
656 cut compressed and cemented Pleistocene sediments in the southern Louisiana where sediment
657 compaction is minimal. Extraction and injection wells, groundwater usage, and other
658 anthropogenic activities may influence subsidence and fault slip.

659 LiDAR differencing can produce trustful results for displacement trends, but LiDAR data must
660 be coregistered to produce accurate results. This method can overestimate displacements, and its
661 accuracy depends on the uncertainty of the available datasets. InSAR time-series are affected by
662 the availability of persistent scatterers in densely vegetated areas and by seasonal changes. Open-
663 source SAR datasets are increasing over time and there will be more sensors in the future (e.g.,

664 NISAR) to expand and improve the time series, and enable selective differencing to minimize
665 seasonal factors.

666 Both methods show that both the footwall and hanging wall of the Baton Rouge fault are
667 subsiding, but the footwall (southern block) is subsiding more slowly. The Baton Rouge fault,
668 therefore, marks a change in vertical crustal movements. LiDAR differencing indicates
669 subsidence with some patches of uplift in the southern block, while the InSAR time series
670 indicates general uplift that reverses the long-term, down-to-the-south displacement, likely
671 InSAR time-series results are affected by hydrological seasonal changes. These trends are
672 consistent with down and southeast motions from the two GNSS stations in the southern block.
673 From the estimated displacement in both blocks we observe creep along the Baton Rouge fault
674 and assume that the fault zone is more permeable and vulnerable to fluid flow than the
675 surrounding areas. Yet, we cannot evaluate the relative contributions of hydrological processes,
676 human intervention, or gravity to the observed fault creep. The Denham Springs fault is not well
677 covered by the LiDAR datasets and shows noise results in the InSAR time series.

678 Given the proximity of extraction and injection wells to areas of vertical crustal motions,
679 anthropological activities such as groundwater withdrawal and injection of fluids are a more
680 reasonable explanation for our observations than geological factors. Our estimations agree with
681 previous groundwater models in the region that indicate a decline in groundwater levels in the
682 East Baton Rouge parish where we found faster subsidence rates. Decay of groundwater levels
683 can cause subsidence and a depression cone at a regional scale. Areas that are locally uplifting in
684 the southern block are nearby injection wells, suggesting that volumetric expansion due to
685 changes in pressure underground is occurring. Considering the future climate change scenarios
686 where population displacement and water scarcity are likely it is important to consider these
687 observations for future city planning to ensure the conservation and protection of the aquifers in
688 the area, and to minimize the effects of saline incursions.

689 **Acknowledgments**

690 CH and CE were supported by funds from the Marshall-Heape endowment to Tulane University,
691 and from training opportunities offered by UNAVCO.

692 CH and CE gratefully acknowledge support from the Marshall-Heape endowment to Tulane
693 University. CH thanks the conversations with J. Whitten about the development of this work.
694 This manuscript benefited from conversations with R. Arrowsmith.

695 **Open Research**

696 **Data Availability Statement**

697 LiDAR data from 1999 is stored and distributed by the Atlas: The Louisiana Statewide GIS
698 (<https://maps.ga.lsu.edu/lidar2000/>), and LiDAR data from 2018 is stored and distributed by the
699 USGS Server through the National Map
700 ([https://rockyweb.usgs.gov/vdelivery/Datasets/Staged/Elevation/LPC/Projects/USGS_LPC_LA_Amit
701 e_2018_LAS_2019/](https://rockyweb.usgs.gov/vdelivery/Datasets/Staged/Elevation/LPC/Projects/USGS_LPC_LA_Amit_e_2018_LAS_2019/)). SAR images from them Envisat satellite were retrieved from the Earth
702 Observation Catalogue (<https://eocat.esa.int/sec/#data-services-area>) and SAR images from
703 Sentinel-1 from the Copernicus Open Access Hub (<https://scihub.copernicus.eu/dhus/#/home>) both
704 property of the European Space Agency. GNSS information was processed by the Nevada Geodetic
705 Laboratory (<http://geodesy.unr.edu/NGLStationPages/gpsnetmap/GPSNetMap.html>). The data from
706 water, injection, and extraction wells is stored in the Strategic Online Natural Resources Information
707 System property of the Louisiana Department of Natural Resources ([http://sonris-
708 www.dnr.state.la.us/gis/agsweb/IE/JSViewer/index.html?TemplateID=181](http://sonris-
708 www.dnr.state.la.us/gis/agsweb/IE/JSViewer/index.html?TemplateID=181)).

709 **Software availability Statement.**

710 LiDAR data was filtered to create stable surface clouds and DEMs were created using the Point
711 Data Abstraction Library (PDAL, 2018). The ICP algorithm was run using the MATLAB code created
712 by Scott et al. (2020) that uses the LIBICP software (Geiger et al, 2012). The Geomorphic Change
713 Detection software (GCD) was used to create the DoDs (Wheaton et al., 2010). InSAR time series
714 were processed using SARscape (2021) software. Spatial analysis and maps were done with QGIS
715 v. 3.18 (2018).

716 **References**

- 717 Anderson, C., Hanor, J., Tsai, F., (2013). Sources of Salinization of the Baton Rouge Aquifer
718 System, Southeastern Louisiana. *Gulf Coast Association of Geological Societies*
719 *Transactions*. 63, 3-12.
- 720 Blewitt, G., Hammond, W., Kreemer, C., (2018), “Harnessing the GPS data explosion for
721 interdisciplinary science”. *Eos*, 99, <https://doi.org/10.1029/2018EO104623>
- 722 Blum, M., & Roberts, H. (2012). The Mississippi delta region: Past, present, and future. *Annual*
723 *Review of Earth and Planetary Sciences*, 40, 655-683. doi:10.1146/annurev-earth-042711-
724 105248
- 725 Brook, A., and Ben-Dor, E., (2011). Automatic Registration of Airborne and Spaceborne Images
726 by Topology Map Matching with SURF processor algorithm. *Remote Sensing*, 3 (1), 65-82.
727 doi:10.3390/rs3010065
- 728 Chan, Y., Koo, V., (2008). An Introduction to Synthetic Aperture Radar (SAR). *Progress in*
729 *Electromagnetics Research*, 2, 27-60. doi:10.2528/PIERB07110101
- 730 Chan, A., and Zoback, A., (2007). The Role of Hydrocarbon production on Land Subsidence and
731 fault reactivation in the Louisiana Coastal Zone. *Journal of Coastal Research*, 23 (3), 771-
732 786. doi: 10.2112/05-0553
- 733 Church, J., Clark, P., Cazenave, A., Gregory, J., Jevrejeva, S., Levermann, A., Merrifield, M.,
734 Milne, G., Nerem, R., Nunn, P., Payne, A., Pfeffer, W., Stammer D., and Unnikrishnan, A.,
735 (2013). Sea Level Change. In: *Climate Change 2013: The Physical Science Basis*.
736 Contribution of Working Group I to the Fifth Assessment Report of the Intergovernmental
737 Panel on Climate Change [Stocker, T., Qin, D., Plattner, G., Tignor, M., Allen, S.,
738 Boschung, J., Nauels, A., Xia, Y., Bex V., Midgley, P., (eds.)]. Cambridge University Press,
739 Cambridge, United Kingdom and New York, NY, USA.
- 740 Crossetto, M., Moserrat, O., Cuevas-Gonzalez, M., Devanthery, N., Crippa, B., (2016). Persistent
741 Scatterer Interferometry: A review. *ISPRS Journal of Photogrammetry and Remote Sensing*.
742 115, 78-89. doi:10.1016/j.isprsjprs.2015.10.011
- 743 Culpepper, D., McDade, E., Dawers, N., Kulp, M., and Zhang, R., (2019a). Synthesis of Fault
744 Traces in SE Louisiana Relative to Infrastructure (Project No. 17GTL SU12). *Transportation*
745 *Consortium of South-Central States*. https://digitalcommons.lsu.edu/transet_pubs/30/
- 746 Culpepper, D., McDade, E., Dawers, N., Kulp, M., and Zhang, R. (2019b). Data from: Synthesis
747 of Fault Traces in SE Louisiana Relative to Infrastructure. Retrieved from
748 https://digitalcommons.lsu.edu/transet_data/30
- 749 Dokka, R. Sella, G., and Dixon, T. (2006). Tectonic control of subsidence and southward
750 displacement of southeast Louisiana with respect to stable North America: *Geophysical*
751 *Research Letters*, 33 (L23308). doi:10.1029/2006GL027250
- 752 Dokka, R. (2011). The role of deep processes in late 20th century subsidence of New Orleans
753 and coastal areas of southern Louisiana and Mississippi. *Journal of Geophysical Research*.
754 116 (B06403). doi:10.1029/2010JB008008.
- 755 Durham, C., and Peeples E., (1956). Pleistocene fault zone in southeastern Louisiana. *Gulf Coast*
756 *Association of Geological Societies Transactions*. 6, 65-66.
- 757 Eddy, D., Van Avendonk, H., Christeson, G., Norton, I., Karner, G., Johnson, C., Snedden, J.,
758 (2014). Deep crustal structure of the northeastern Gulf of Mexico: Implications for rift

- 759 evolution and seafloor spreading. *Journal of Geophysical Research: Solid Earth*. 119 (9),
760 6802-6822. doi: 10.1002/2014JB011311
- 761 Elshall, A., Tsai, F., Hanor, J., (2013). Indicator geostatistics for reconstructing Baton Rouge
762 aquifer-fault hydrostratigraphy, Louisiana, USA. *Hydrogeological Journal*. 21 (8), p. 1731-
763 1747. doi: 10.1007/s10040-013-1037-5
- 764 European Space Agency, (ESA) (2021a). Earth Observation Catalogue – EO CAT. EnviSAT
765 images. Last visited July/2022. Retrieved from <https://eocat.esa.int/sec/#data-services-area>
- 766 European Space Agency, (ESA) (2021b). Copernicus Open Access Hub. Sentinel-1 images. Last
767 visited July/2022. Retrieved from <https://scihub.copernicus.eu/dhus/#/home>
- 768 Ferretti, A., Prati, C., Rocca, F., (2001) Permanent scatterers in SAR interferometry. *IEEE*
769 *Transactions on Geoscience and Remote Sensing*. 39 (1), 8–20. doi:10.1109/36.898661
- 770 Fiaschi, S., and Wdowinski, S., (2020). Local land subsidence in Miami Beach (FL) and Norfolk
771 (VA) and its contribution to flooding hazard in coastal communities along the U.S. Atlantic
772 coast. *Ocean and Coastal Management*. 187. doi:10.1016/j.ocecoaman.2019.105078
- 773 Frederikse, T., Landerer, F., Caron, L. Adhikari, S., Parkes, D., Humphrey, V., Dangendorf, S.,
774 Hogarth, P., Zanna, L., Cheng, L., and Wu, Y., (2020). The causes of sea-level rise since
775 1900. *Nature*. 584 (7821), 393–397. doi:10.1038/s41586-020-2591-3
- 776 Gagliano, S., Burton Kemp III, E., Wicker, K., and Wiltenmuth, K., (2003a). Active geological
777 faults and land change in southeastern Louisiana (Contract No. DACW 29-00-C-0034). *U. S.*
778 *Army Corps of Engineers*. <https://biotech.law.lsu.edu/katrina/govdocs/faults.pdf>
- 779 Gagliano, S., Burton Kemp III, E., Wicker, K., Wiltenmuth, K., and Sabate, R., (2003b). Neo-
780 tectonic framework of southeast Louisiana and applications for Coastal restoration.
781 *Transactions of the 53rd The Gulf Coast Association of Geological Societies and the Gulf*
782 *Coast Section SEMP*. 262-272
- 783 Gasparini, N, Fischer, G, Adams, J, Dawers, N., Janoff, A., (2015) Morphological signatures of
784 normal faulting in low-gradient alluvial rivers in South-eastern Louisiana, USA. *Earth*
785 *Surface Processes and Landforms*. 41, 642-657. doi: 10.1002/esp.3852
- 786 Geiger, A., Lenz, P., and Urtasun, R., (2012). Are we ready for autonomous driving the kitti
787 vision benchmark suite. 2012 IEEE Conference on Computer Vision and Pattern
788 Recognition. 3354-3361. doi: 10.1109/CVPR.2012.6248074. [Computer software]
789 <http://www.cvlibs.net/software/libicp/>
- 790 Goldstein, R., Zebker, H., Werner, C., (1988). Satellite radar interferometry: Two-dimensional
791 phase unwrapping. *Radio Science*. 23 (4), 713-720. doi:10.1029/RS023i004p00713
- 792 Guzy, A., Malinowska, A., (2020). State of the art and recent advancements in the modelling of
793 land subsidence induced by groundwater withdrawal. *Water*. 12 (7). doi:10.3390/w12072051
- 794 Hoffman, J., Keyes, D., Titus, J., (1983). Projecting Future Sea Level Rise: Methodology,
795 Estimates to the Year 2100, and Research Needs. United States: Strategic Studies Staff,
796 Office of Policy Analysis, Office of Policy and Resource Management, U.S. Environmental
797 Protection Agency. Retrieve from <https://repository.library.noaa.gov/view/noaa/10299>
- 798 Hooper, A., Zebker, H., Segall, P., Kampes, b., (2004). A new method for measuring deformation
799 on volcanoes and other natural terrains using InSAR persistent scatterers. *Geophysical*
800 *Research Letters*. 31 (23), L23611. doi:10.1029/2004GL021737.

- 801 Hopkins, M., Lopez, J., Songy, A., (2021). Coastal Subsidence Due to Faults: Insights from
802 Elevation Profiles of Vehicular Bridges, Southeastern Louisiana, U.S.A. *Journal of Coastal*
803 *Research*. 38(1), 52-65. doi:10.2112/JCOASTRES-D-21-00015.1
- 804 Jankowski, K., Törnqvist, T., Fernandes, A., (2017) Vulnerability of Louisiana's coastal wetlands
805 to present-day rates of relative sea-level rise. *Nature Communication*. 8 (14792).
806 doi:10.1038/ncomms14792
- 807 Jones, C., An, K., Blom, R., Kent, J., Ivins, E., and Bekaert, D. (2016). Anthropogenic and
808 geologic influences on subsidence in the vicinity of New Orleans, Louisiana. *Journal of*
809 *Geophysical Research: Solid Earth*. 121 (5), 3867– 3887. doi:10.1002/2015JB012636
- 810 Karegar, M., Dixon, T., Malservisi, R., (2015). A three-dimensional surface velocity field for the
811 Mississippi Delta. Implications for coastal restoration and flood potential. *Geology*. 43 (6),
812 519-522. doi:10.1130/G36598.1
- 813 Karegar, M., Dixon, T., Malservisi, R., Kushe, J., and Engelhart, S., (2017) Nuisance flooding
814 and relative Sea-Level Rise: the importance of present-day land motion. *Science Reports*. 7
815 (111997). doi:10.1038/s41598-017-11544-y
- 816 Karegar, M., Larson, K., Kushe, J., and Dixon, T., (2020) Novel quantifications shallow sediment
817 compaction by GPS Interferometric Reflectometry and implications for flood susceptibility.
818 *Geophysical Research Letters*. 47 (14). doi:10.1029/2020GL087807
- 819 Keogh, M., and Törnqvist, T., (2019). Measuring rates of present-day relative sea-level rise in low
820 elevation coastal zones. *Ocean Science*, 15 (1), 61-73. doi:10.5194/os-15-61-2019
- 821 Kuchar, J., Milne, G., Wolstencroft, M., Love, R., Taarasov, L., and Hijma, M., (2018). The
822 Influence of Sediment Isostatic Adjustment on Sea Level Change and Land Motion Along
823 the U.S. Gulf Coast: *Journal of Geophysical Research*, 123 (1), 780-796.
824 doi:10.1002/2017JB014695
- 825 Kuecher, G., Roberts, H., and Thompson, M., (2001). Evidence for Active Growth Faulting in the
826 Terrebone Delta Plain, South Louisiana: Implications for Wetland loss and the Vertical
827 Migration of Petroleum. *Environmental Geosciences*, 8 (2), 77-94. doi:10.1046/j.1526-
828 0984.2001.82001.x
- 829 Kulp, S., and Strauss, B., (2019). New elevation data triple estimates of global vulnerability to
830 sea-level rise and coastal flooding. *Nature Communications*. 10 (4844). doi:10.1038/s41467-
831 019-12808-z
- 832 L3Harris. (2014, November). PS Tutorial – version 0.9. Retrieved April 17, 2022, from
833 https://www.sarmap.ch/tutorials/PS_Tutorial_V_0_9.pdf
- 834 L3Harris. (2021, August). PS Tutorial – version 5.6. Retrieved April 17, 2022, from
835 https://www.sarmap.ch/tutorials/PS_v56.pdf
- 836 Li, J., Wang, S., Miche, C., Russell, H., (2020). Surface deformation observed by InSAR shows
837 connections with water storage change in Southern Ontario. *Journal of Hydrology: Regional*
838 *Studies*. 27, 100661- 100672. doi:10.1016/j.ejrh.2019.100661
- 839 Lillesand, T. and Kiefer, R., (2000). Remote Sensing and image interpretation. John Wiley &
840 Sons, New York.
- 841 Love, R., Milne, G., Tarasov, L., Engelhart, S., Hijma, M., Latychev, K., Horton, B., and
842 Törnqvist, T., (2016). The Contribution of Glacial Isostatic Adjustment to projections of Sea-

- 843 level change along the Atlantic and Gulf coast of North America. *Earth's Future*. 4 (10), 440-
844 464. doi:10.1002/2016EF000363
- 845 Louisiana Department of Natural Resources – Strategic Online Natural Resources Information
846 System (SONRIS), (n.d.). Data of: Oil/Gas wells, Injection wells, and Water wells
847 registration [shp format], last visited June/2020. Retrieved from: [http://sonris-
www.dnr.state.la.us/gis/agsweb/IE/JSViewer/index.html?TemplateID=181](http://sonris-
848 www.dnr.state.la.us/gis/agsweb/IE/JSViewer/index.html?TemplateID=181)
- 849 Louisiana State University - Department of Geography and Anthropology (LSU), (n.d.). LiDAR
850 data distribution by “Atlas: The Louisiana Statewide GIS.” [LAS format], Baton Rouge, LA.
851 Last visited: June/2020. Retrieved from: <http://atlas.lsu.edu>.
- 852 Lyons, S., and Sandwell, D., (2003). Fault creep along the southern San Andreas from
853 interferometric synthetic aperture radar, permanent scatterers, and stacking. *Journal of
854 Geophysical Research: Solid Earth*. 108 (B1), 11-24. doi:10.1029/2002JB001831
- 855 McCulloh, R., (2001) Active Faults in East Baton Rouge Parish; Louisiana. *Louisiana Geological
856 Survey*. Public information series n. 8. Available at
857 <https://www.lsu.edu/lgs/publications/products/public-information-series.php> (Accessed:
858 January 2020)
- 859 Milliman J., Haq B., (1996). “Sea-Level Rise and Coastal Subsidence: Towards Meaningful
860 Strategies” In: Milliman, J.D., Haq, B.U. (eds) Sea-Level Rise and Coastal Subsidence.
861 Coastal Systems and Continental Margins, vol 2. Springer, Dordrecht. 1-9. doi:10.1007/978-
862 94-015-8719-8_1
- 863 Morton, R., Busteri, N., Dennis K. (2002). Subsidence Rates and Associated Wetland Loss in
864 South-Central Louisiana. *Transactions of the Gulf Coast Association of Geological Societies*.
865 52, 767-778.
- 866 Nasreen, M. (2003) The Effect of Faults upon Ground Water Flow in the Baton Rouge Fault
867 System. [master’s thesis]. [New Orleans (LA)] University of New Orleans. Available at
868 <https://scholarworks.uno.edu/td/54> (Accessed: 1 June 2022)
- 869 National Academies of Sciences, Engineering, and Medicine (NASEM), (2018a). Thriving on
870 Our Changing Planet: A Decadal Strategy for Earth Observation from Space. Washington,
871 DC: The National Academies Press. doi:10.17226/24938.
- 872 National Academies of Sciences, Engineering, and Medicine (NASEM), (2018b). Understanding
873 the Long-Term Evolution of the Coupled Natural-Human Coastal System: The Future of the
874 U.S. Gulf Coast. Washington, DC: The National Academies Press. doi:10.17226/25108
- 875 National Geodetic Survey (n.d.). Data from: Finding Survey Marks and Datasheets - LA[shp
876 format], last visited January/2020. Retrieved from
877 https://geodesy.noaa.gov/pub/DS_ARCHIVE/BETA_PRODUCTS/
- 878 Nerem, R., Beckley, B., Fasullo, J., Hamlington, B., Masters, D., Mitchum, G., (2018). Climate-
879 change–driven accelerated sea-level rise detected in the altimeter era. *Proceedings of the
880 National Academy of Sciences*. 115 (9), 2022-2025. doi:10.1073/pnas.1717312115
- 881 Neverman, A., Fuller, I. (2016). Application of Geomorphic Change Detection (GCD) to quantify
882 morphological budgeting error in a New Zealand gravel-bed river: a case study from the
883 Makaroro River, Hawke’s Bay. *Journal of Hydrology*. 55 (1), 45-63. Available at
884 <https://www.jstor.org/stable/43945085> (Accessed: 21 October 2021)

- 885 Nienhuis, J., Törnqvist, T., Jankowski, K., Fernandes, A., Keogh, M., (2017). A New Subsidence
886 Map for Coastal Louisiana. *GSA Today*. 27 (9), 58-59. doi:10.1130/GSATG337GW.1
- 887 Nissen, E., Krishnan, A., Arrowsmith, R., Saripalli, S., (2012). Three-dimensional surface
888 displacements and rotations from differencing pre-and post-earthquake LiDAR point clouds.
889 *Geophysical Research Letters*, 39 (16). doi:10.1029/2012GL052460
- 890 PDAL Contributors, (2018). PDAL Point Data Abstraction Library. doi:10.5281/zenodo.2556738
- 891 Pendleton, E., Barras, J., Williams, S., Twichell, D., (2010). Coastal vulnerability assessment of
892 the Northern Gulf of Mexico to sea-level rise and coastal change. *U.S. Geological Survey*.
893 Open-File Report. doi:10.3133/ofr20101146
- 894 Penland, S. and Ramsey, K., (1990). Relative Sea Level Rise in Louisiana and the Gulf of
895 Mexico: 1908-1988. *Journal of coastal Research*. 6 (2), 323-342. Available at
896 <https://www.jstor.org/stable/4297682> (Accessed: 20 Marzo 2021)
- 897 Penland, S., Beall, A., and Waters, J., (2001) Environmental atlas of the Lake Pontchartrain
898 Basin. *U.S. Geological Survey*. Open-File Report 02-206. Retrieve from
899 <https://pubs.usgs.gov/of/2002/of02-206/intro/toc.html>
- 900 Pindell, J. Kennan, L., (2009), Tectonic evolution of the Gulf of Mexico, Caribbean and northern
901 South America in the mantle reference frame: An update. In *The Origin and Evolution of the*
902 *Caribbean Plate, Geological Society, Special Publication.*, edited by Lorente, J., Pindell, J.
903 328, 1–55. doi:10.1144/SP328.1.
- 904 Polat, N., Uysal, M., Toprak, A., (2015). An investigation of DEM generation process based on
905 LiDAR data filtering, decimation, and interpolation methods for an urban area.
906 Measurement. *Journal of the International Measurement Confederation*. 75, 50-56.
907 doi:10.1016/j.measurement.2015.08.008
- 908 Puskas, C., Meertens, C., & Phillips, D. (2017). Hydrologic loading model displacements from
909 the National and Global Data Assimilation Systems (NLDAS and GLDAS). *UNAVCO*
910 *Geodetic Data Service Group*.
- 911 Qiang, Y., Lam, N., (2016). The impact of Hurricane Katrina on urban growth in Louisiana: an
912 analysis using data mining and simulation approaches. *International journal of Geographical*
913 *Information Science*. 30 (9), 1832-1852. doi:10.1080/13658816.2016.1144886
- 914 QGIS Development Team, 2018. QGIS Geographic Information System. Open-Source Geospatial
915 Foundation Project. [computer software] <http://qgis.osgeo.org>
- 916 SARscape [computer software] (2021). Boulder, Colorado
- 917 Sastry, N., (2009). Tracing the Effects of Hurricane Katrina on the Population of New Orleans:
918 The Displaced New Orleans Residents Pilot Study. *Sociological Methods and Research*. 38
919 (1), 171-196. doi:10.1177/0049124109339370
- 920 Sawyer, D., Buffler, R., Pilger Jr., R., (1991), “The crust under the Gulf of Mexico basin” In *The*
921 *Gulf of Mexico Basin*, Geological Society of America, ed. by A. Salvador. 53–72.
922 doi:10.1130/DNAG-GNA-J.53
- 923 Scott, C., Arrowsmith, J., Nissen, E., Lajoie, L., Maruyama, T., Chiba, T., (2018). The M7 2016
924 Kumamoto, Japan, Earthquake: 3-D deformation along the fault and within the damage zone
925 constrained from Differential Lidar Topography. *Journal of Geophysical Research: Solid*
926 *Earth*, 123 (7) 6138-6155. doi:10.1029/2018JB015581

- 927 Scott, C., Phan, M., Nandigam, V., Crosby, C., & Arrowsmith, R. (2020). On-Demand 3D
928 topographic differencing implemented in OpenTopography (Version 1.1.0) [Computer
929 software]. https://github.com/OpenTopography/3D_Differencing
- 930 Shen, Z., Dawers, N., Törnqvist, T., Gasparini, N., Hijma, M., and Mauz, B. (2017). Mechanism
931 of late Quaternary fault throw-rate variability along the north central Gulf of Mexico coast:
932 implication for coastal subsidence. *Basin Research*. 29 (5), 557-570. doi:10.1111/bre.12184
- 933 Shepard, D., (1968). A two-dimensional interpolation function for irregularly spaced data.
934 Proceedings of the 1968 ACM National Conference. 517 – 524.
935 <https://doi.org/10.1145/800186.810616>
- 936 Shirzaei, M., Ellsworth, W., Tiampo, K., Gonzalez, P., Manga, M., (2016). Surface uplift and
937 time-dependent seismic hazard due to fluid injection in eastern Texas. *Science*. 353 (6306),
938 1416-1419. doi:10.1126/science.aag0262
- 939 Simons, M., Rosen, P., (2015). “Interferometric Synthetic Aperture Radar Geodesy.” In Gerald
940 Schubert (editor-in-chief) *Treatise on Geophysics*, 2nd edition, Vol 3. Oxford: Elsevier. 339-
941 385
- 942 Stevenson, D. A., & Agnew, J. D. (1988). Lake Charles, Louisiana, earthquake of 16 October
943 1983. *Bulletin of the Seismological Society of America*. 78 (4), 1463-1474.
944 doi:10.1785/BSSA0780041463
- 945 Teatini, P., Gambolati, G., Ferronato, M., Serrati, A., Walters, D., (2011). Land uplift due to
946 subsurface fluid injection. *Journal of Geodynamics*. 51 (1), 1-16.
947 doi:10.1016/j.jog.2010.06.001
- 948 Tomaszewski, D., Lovelace, J., Ensminger, P., (2002). Water withdrawals and trends in
949 groundwater levels and stream discharge in Louisiana. *Louisiana Department of*
950 *Transportation and Development, and U.S. Geological Survey*, technical report No. 68.
- 951 Turner, R., Rabalais, N., (2018). “The Gulf of Mexico.” In *World Seas: An Environmental*
952 *Evaluation (Second Edition)*, Academic Press -Elsevier, edited by Sheppard, C, 445-464.
953 doi:10.1016/B978-0-12-805068-2.09994-0
- 954 United States Army Corps of Engineers (USACE) (2001). Data from: Raw LIDAR Elevation
955 Data, UTM 15 NAD83, Louisiana FEMA Project - Phase 1: Amite River Basin. last visited
956 June/2020 Retrieve from: <https://maps.ga.lsu.edu/lidar2000/>
- 957 United States Geological Survey (USGS) (2019), USGS Lidar Point Cloud LA Amite 2018, [LAZ
958 format], last visited July/2022. Retrieve from:
959 [https://rockyweb.usgs.gov/vdelivery/Datasets/Staged/Elevation/LPC/Projects/USGS_LPC_L](https://rockyweb.usgs.gov/vdelivery/Datasets/Staged/Elevation/LPC/Projects/USGS_LPC_LA_Amite_2018_LAS_2019/)
960 [A_Amite_2018_LAS_2019/](https://rockyweb.usgs.gov/vdelivery/Datasets/Staged/Elevation/LPC/Projects/USGS_LPC_LA_Amite_2018_LAS_2019/)
- 961 U.S. Census Bureau. (2003, October). Louisiana 2000 – Population and Housing units counts
962 (Report No. PHC-3-20). Retrieved from
963 <https://www2.census.gov/library/publications/2003/dec/phc-3-20.pdf>
- 964 U.S. Census Bureau. (2012, July). Louisiana 2010 – Population and Housing units counts (Report
965 No. CPH-2-20). Retrieved from
966 <https://www2.census.gov/library/publications/decennial/2010/cph-2/cph-2-20.pdf>
- 967 U.S. Census Bureau. (2021, August). 2020 Population and Housing State Data. Retrieved from
968 [https://www.census.gov/library/visualizations/interactive/2020-population-and-housing-state-](https://www.census.gov/library/visualizations/interactive/2020-population-and-housing-state-data.html)
969 [data.html](https://www.census.gov/library/visualizations/interactive/2020-population-and-housing-state-data.html)

- 970 Vahdat-Aboueshagh, H., Tsai, F., (2021). Constructing large-scale complex aquifer systems with
971 big well log data: Louisiana model. *Computers and Geosciences*. 148, 104687.
972 doi:10.1016/j.cageo.2021.104687
- 973 Walter, J. I., Dotray, P. J., Frohlich, C., & Gale, J. F. (2016). Earthquakes in northwest Louisiana
974 and the Texas–Louisiana border possibly induced by energy resource activities within the
975 Haynesville shale play. *Seismological Research Letters*. 87(2A), 285-294.
976 doi:10.1785/0220150193
- 977 Wheaton, J., Brasington, J., Darby, S., Sear, D., (2010). Accounting for uncertainty in DEMs
978 from repeat topographic surveys: improved sediment budgets. *Earth Surface processes and
979 Landforms*. 35 (2), 136-156. doi:10.1002/esp.1886 [computer software]
980 <https://github.com/Riverscapes/gcd>
- 981 Wheaton, J., (2018). Principles of topographic change detection. EarthCube Advancing the
982 Analysis of HRT Workshop Advancing the Analysis of High-Resolution Topography,
983 Broomfield, CO. August 21-24.
984 https://www.youtube.com/watch?v=QIoK52W5sUM&ab_channel=OpenTopography (last
985 accessed November 10, 2020)
- 986 White, E. (2017). Water Resources of the Southern Hills Regional Aquifer System, Southeastern
987 Louisiana. *U.S. Geological Survey Fact Sheet* 2017–3010. doi:10.3133/fs20173010
988
- 989